Master Erasmus Mundus in Photonics Engineering, Nanophotonics and Biophotonics

Europhotonics

MASTER THESIS WORK

Optical Detection of Mechanical Motion of Graphene by Light-Matter Interactions

Kevin Gerd Schädler

Supervised by Prof. Frank Koppens (Institut de Ciències Fotòniques, ICFO) and Prof. Uli Lemmer (Light Technology Institute, Karlsruhe Institute of Technology, KIT)

Presented September 1st 2012 in Barcelona

Registered at

Escola Tècnica Superior d'Enginyeria de Telecomunicació de Barcelona

Abstract

In this thesis, we study both experimentally and theoretically the optical detection of the motion of graphene membranes based on fluorescence quenching of the emitters close to graphene. Fluorescence quenching occurs due to distance-dependent resonant energy transfer from the emitter dipoles to electron-hole dipoles in the graphene, and may be detected by lifetime measurement of the emitters. Nanoresonators consisting of graphene suspended over hole and trench structures coated with quantum dots are fabricated and their surface and emission properties characterised. The membranes are actuated electrostatically, and their movement is detected both mechanically by atomic force microscopy and also by lifetime measurements of the quantum dots.

Contents

1 Introduction

Graphene is an atomically thin material composed of carbon atoms arranged in a honeycomb lattice. Its extraordinary properties give rise to many studies since Novoselov and Geim showed that free-standing flakes of the material exist in 2004 [1]. Having been predicted theoretically long beforehand, many optoelectronic properties such as its conical band structure for low energies, ambipolar field effect, universal absorption and relativistic charge carriers as well as its high mechanical stiffness are now accessible experimentally and can be exploited in a host of fields and applications, the list of which is still growing to date.

The optoelectronic properties of graphene have brought it to be used in devices such as ultra high-gain photodetectors [2] and ultra-fast transistors [3] with superior properties compared to their semiconductor counterparts. Its high conductivity and transmittivity allow it to be used as as a transparent electrode in photovoltaics, light-emitting devices and displays [4]. Considering these applications, a further advantage is that graphene can now also be produced in large area sheets [5] at competitive costs compared to the transparent conductors used today, while providing more mechanical stability.

In terms of fundamental physics, graphene's transport properties resemble those of a two-dimensional electron gas (2DEG) with massless charge carriers described by the relativistic Dirac equation that move ballistically over the large mean free path of the order of 100s of nanometres [6] in the lattice. These properties allow for studies of the behaviour of quantum phenomena at room temperature, such as the quantum Hall effect [7] and quantized minimum conductivity $\sigma \approx \frac{h}{4e^2}$ even for very low carrier densities[8, 9], amongst others. Its universal optical absorbance of $\pi\alpha \approx 2.3\,\%$ is related to a fundamental constant, the fine structure constant $\alpha = \frac{e^2}{h}$ [10], making it visible to the naked eye despite being atomically thin.

Graphene's mechanical properties combined with its thickness make it very attractive to study resonators with the thinnest and stiffest material ever measured [11]. Owing to these properties, nano-resonators with ultra-high quality factors have been extensively studied and characterised [12, 13, 14, 15]. These nanoresonators display resonance frequencies in the range of MHz which are very sensitive to changes of the membrane structure, making them ultra-sensitive mass and pressure sensors [12].

Recently, it has been proposed that graphene can also be used as a fundamental ruler by measuring the distance of a graphene sheet to a fluorescent emitter [16]. This is based on a theoretical model which predicts that graphene is highly efficient in quenching the fluorescence of nearby emitters by resonant energy transfer from the fluorophore to the

sheet. The high degree of quenching is surprising, given that graphene is so thin and shows only weak interaction with incident electromagnetic fields. The excited state lifetime, and with it the radiative decay rate is expected to show a d^{-4} dependence on the separation d of the emitter from the graphene. Therefore, it is possible to determine this distance by a non-contact optical measurement of the emitter's fluorescent lifetime.

1.1 State of the Art

To date, it has been demonstrated that graphene quenches the fluorescence intensity of fluorescent molecules [17], semiconductor quantum dots [18] and individual semiconductor nanocrystals [19]. This quenching is attributed to fluorescence resonance energy transfer between dipoles of the emitters and the electron-hole dipole in graphene, and is detected by measurement of the emission intensity change in the presence of graphene.

The distance dependence of the resonant energy transfer process and the associated change non-radiative decay rate has been theoretically studied for the case of a dye molecule in close proximity to graphene [20, 21], considering out-of-plane dipole excitations of the graphene by the emitting dipole. In a more detailed theoretical study, the in-plane excitations were also considered, proposing different regimes of distance dependence [16], with a dominating d^{-4} dependence for separations below 30 nm being predicted.

An experimental study has recently shown good agreement with the theory proposed [22]. Graphene was separated from a thin layer of fluorescent molecules by dielectric spacing layers of variable thickness to detect distance dependence. In contrast to previous work, this study used a measurement of the change of the emitter's lifetime instead of fluorescent emission, making it independent of factors such as the photobleaching of the emitters which can also change the emitted intensity. However, the distances probed by this method are discrete and rely on an accurate determination of the separator thickness.

Sheets of graphene suspended on nanoscale support structures have been shown to be deflectable by mechanical [14] or electrostatic force [12] to study their mechanical properties. These structures form resonators which can be produced on a large scale [23], and exhibit high resonance frequencies and quality factors [13] upon electrical or optical excitation [24].

1.2 Goals

The primary goal of this thesis is to optically detect the mechanical motion of graphene nano-mechanical resonators. The optical detection relies on the quenching of fluorescence by resonant energy transfer from emitters to a graphene sheet in close proximity. The degree of quenching depends on the separation of the graphene sheet and the emitters, therefore a measurement of fluorescence quenching allows for the determination of this distance after calibration. A method of varying the distance of a graphene sheet to fluorescing emitters is to be developed and experimentally verified.

The combination of the electrostatic deflection of a graphene membrane on a resonator structure together with its fluorescence quenching properties allow the membrane motion to be detected by optical measurement of the emission and excited state lifetime of nearby emitters. Furthermore, this approach allows for a continuous range of separations between the emitter and the sheet, enabling a more accurate determination of how the graphene-emitter interaction scales with distance.

2 Preliminary Notions

2.1 The Electronic and Optical Properties of Graphene

2.1.1 Band Structure, Charge Carriers and Ambipolar Electric Field Effect

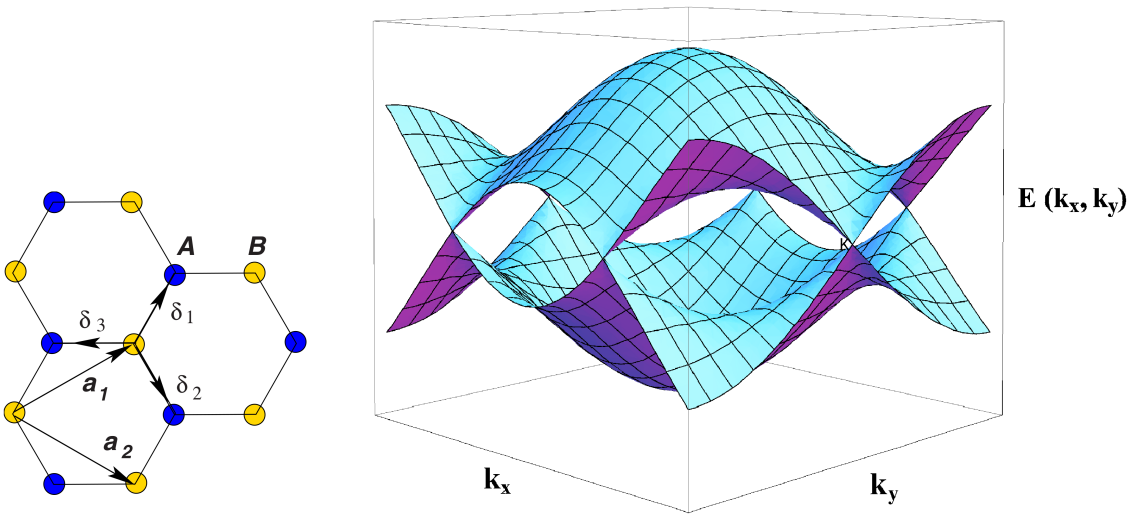

(a) (b)

Figure 1: (a) Graphene lattice structure composed of carbon atoms arranged in hexagonal rings linked together. Elements of the two sub-lattices A (blue) and B (yellow) are also shown, together with a set of lattice vectors $(\boldsymbol{a}_1, \boldsymbol{a}_2)$ and the three nearest-neighbour vectors $\boldsymbol{\delta}_1$, $\boldsymbol{\delta}_2$, $\boldsymbol{\delta}_3$. Source: [25] (b) Graphene band structure $E(k_x, k_y)$ in the first Brillouin zone showing the conduction (top) and valence (bottom) bands together with the six Dirac ($\mathbf{K}$) points that form the Fermi surface. Source: [20]

Many of graphene's outstanding optoelectronic properties arise from its two-dimensional lattice structure of carbon atoms joined together to form a hexagonal lattice, as shown in Fig. 1a. The lattice can be subdivided into two sub-lattices A and B, each spanned by lattice vectors $\boldsymbol{a_1}$ and $\boldsymbol{a_2}$ and interconnected by nearest-neighbour vectors $\boldsymbol{\delta}_1$, $\boldsymbol{\delta}_2$ and $\boldsymbol{\delta}_3$. In this chapter, some of the properties related to the experiments performed in this thesis will be discussed. However, this is by no means an exhaustive list, the interested reader is referred to reviews such as those by Castro-Neto et al. [25] , Cooper et al. [26] and Bonaccorso et al. [4] for more details and references.

One of graphene's most prominent features is its gap-less, linear band structure. This band structure was first studied by Wallace in 1947 [27], at a time when graphene was still just a theoretical notion, and the existence of two-dimensional (2D) solids was considered impossible due to their thermodynamic instability [28]. Wallace proposed

the idea of modeling the electronic structure of graphene with a tight-binding Hamiltonian, which only considers first-nearest-neighbour interactions and the π-bonds between atoms, thus greatly simplifying the calculation. The result of this is the following dispersion relation [4]:

$$E^{\pm}(k_x, k_y) = \pm\gamma_0\sqrt{1 + 4\,cos(\frac{\sqrt{3}k_x a}{2})\,cos(\frac{k_y a}{2}) + 4\,cos^2(\frac{k_y a}{2})} \tag{1}$$

where E^+ and E^- denote the energy of the conduction and valence bands, respectively. The term γ_0 denotes the tunneling between nearest-neighbour π-orbitals and a is the distance between equivalent points in the carbon lattice, given as $a = \sqrt{3}a_{cc}$, where $a_{cc} = 1.42\,\mathring{A}$ is the carbon-carbon atomic separation. Equation 1 is visualized in 1b inside the first Brillouin zone for k_x and k_y, which can be linearly combined to form the lattice momenta: $\mathbf{k} = (k_x, k_y)$. There are six distinct points in 1b where $E^+ = E^-$, these are the so-called Dirac points at which the density of charge carriers is zero. These points define a plane which is associated with the so-called Dirac energy. In the case of undoped graphene, the Dirac and Fermi energies are equal. One can expand 1 around the Dirac points with location $\mathbf{K}$ to obtain the following expression [4]:

$$E^{\pm}(\boldsymbol{\kappa}) \approx \pm\hbar\nu_F|\boldsymbol{\kappa}|$$

with $\boldsymbol{\kappa} = \mathbf{k} - \mathbf{K}$ and $\nu_F = \sqrt{3}\gamma_0 a/(2\hbar) \approx 10^6\,m\,s^{-1}$ the Fermi velocity, which is constant in the linear dispersion regime. This cone-shaped band structure is linear within approximately 1 eV from the Dirac points [26] and is shown in Fig. figure 2a. The linear dispersion causes the charge carriers in this region of reciprocal space to have zero effective mass. This is due to the relation

$$m^* \propto \frac{d^2\,E}{d\,k^2} = 0,\; E \approx E_F$$

which yields charge carriers with $m^* = 0$. These are termed massless Dirac fermions owing to their simpler description by the relativistic Dirac equation - due to their linear dispersion relation - instead of the Schrödinger equation. This however does not imply that these particles are actually relativistic [9, 8]. They move through the graphene lattice ballistically over distances up to $0.3\,\mu m$ with mobilities exceeding $15000\,cm^2\,V^{-1}\,s^{-1}$, at room temperature [8], with even higher mobilities of $200,000\,cm^2\,V^{-1}\,s^{-1}$ recorded for suspended graphene [29].

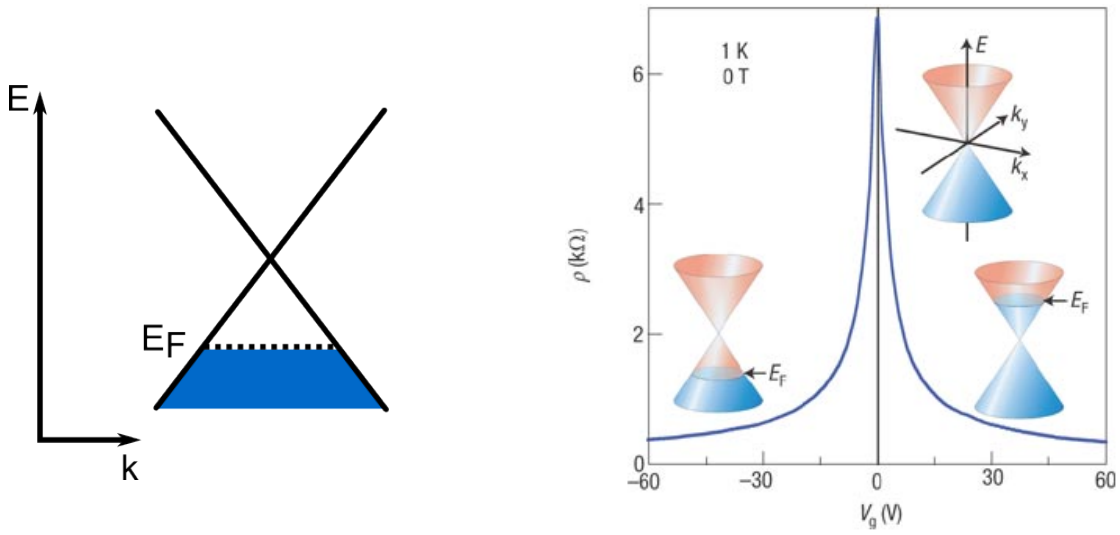

(a) (b)

Figure 2: (a) Linear dispersion relation and Fermi energy in graphene (b) Ambipolar electric field effect in graphene. A maximum of resistivity (Dirac peak) occurs at $V_g = 0\,V$ for undoped graphene, as the number of charge carriers reaches a minimum here. Insets: conical, low energy band structure $E(\mathbf{k})$ with two different, gate voltage dependent doping levels. By varying the gate voltage V_g, the density and polarity of free charges in graphene can be modified, accompanied by a change in Fermi level E_F. Positive gate voltages induce electron doping, while negative voltages induce hole doping. Source: [8].

The density of charge carriers in graphene can be modified by the ambipolar electric field effect [1], which means that graphene can be doped by applying a gate voltage to it - this causes a shift of the Fermi level. Fig. 2b shows the ambipolar field effect, whereby the application of a backgate voltage V_g changes the density of charges and thus the resistivity of graphene. The relation between the change in charge density n and the applied gate voltage V_g is linear and given by:

$$n = \epsilon_0\,\epsilon\,V_g/t\,e$$

where ϵ_0 is the permittivity of free space, ϵ is the relative permittivity of the dielectric substrate on which the graphene is placed to electrically isolate it from the gate, and t is the substrate thickness, i.e. the distance between the graphene and the gate. For $V_G = 0$, the density of charges is zero, therefore the the resistivity reaches a maximum (Dirac peak). The Fermi energy E_F is proportional to the square root of the density of charges: $E_F = \hbar\nu_F\sqrt{\pi n}$ [1] , thus it can be tuned by applying a gate voltage V_g - this is shown in the inset of Fig. figure 2b.

Having discussed some of the prominent electronic features of graphene, the focus shall now be on its optical properties, both of which are closely related.

2.1.2 Constant Absorption

It has been predicted theoretically and shown experimentally that graphene features universal absorption across a wide range of wavelengths, solely defined by the fine structure constant $\alpha = \frac{e^2}{hc} \approx 1/137$, e being the electron charge, c the speed of light in vacuum and h Planck's constant. Despite being only one atomic layer thick, a single layer of graphene is found to absorb a considerable and constant amount of radiation across the visible spectrum (approximately $400 - 700\,nm$), given by $\pi\,\alpha \approx 2.3\%$ [10]. This is shown in Fig. 3, where a multilayer graphene flake is partially suspended over a metal aperture, and optical transmittance measurements under white-light illumination are performed. From the transmittance measurements, one can clearly see how the monolayer absorbs 2.3 % of the light, whereas the bilayer absorbs twice this fraction. Other experiments have shown the absorption of graphene to be flat across in an even larger wavelength range from $300\,nm - 2500\,nm$ [4].

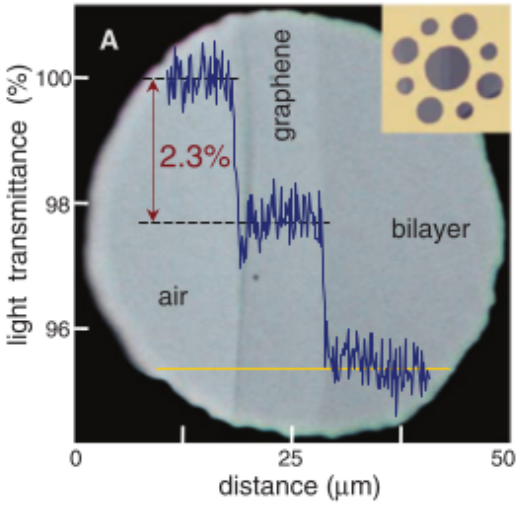

Figure 3: Optical transmittance of single and bilayer graphene. Shown are the measured data and the optical image (background) of single and bilayer graphene under white light illumination. Each layer absorbs approximately 2.3 % of the incident light, making the atomically thin layers visible to the naked eye. Inset: metal mask structure used to support the multilayer graphene flake in the image. Source: [10]

2.1.3 Non-Radiative Energy Transfer

Fluorescence is an example of a spontaneous emission process whereby an emitter such as an atom - assumed to be initially in an excited state - decays to its ground state by emitting a photon, which is a radiative decay process. Being quantum-mechanical in nature, the event of the excited atom emitting a photon occurs at some random time which cannot be exactly predicted. However, through quantum mechanics it is possible to calculate the probability of decay for an emitter - this is given by Fermi's Golden Rule [30]:

$$\Gamma_{ij} \propto |M_{ij}|^2 \rho(\omega_{ij}) \tag{2}$$

This equation describes the dependence of the transition or decay rate Γ_{ij} between a state i and a state j on the transition matrix element M_{ij} derived from the electric dipole interaction and the optical density of states $\rho(\omega_{ij})$ at the transition frequency ω_{ij}, which is determined by the energy difference $E_{ij} = \hbar\omega_{ij}$ between states i and j. This decay rate has a decay time $\tau_{ij} = \Gamma_{ij}^{-1}$ associated with it, which is a characteristic time describing the time that an emitter is in the state i before the transition to state j. From equation 2 , we see that the rate of radiative decay could be altered by modification of M_{ij} or $\rho(\omega_{ij})$. In general, M_{ij} is given by

$$M_{ij} = \langle\, j \,|\, H \,|\, i \,\rangle = \int \psi_j^*(\mathbf{r})\, H(\mathbf{r})\, \psi_i(\mathbf{r})\, d^3\mathbf{r}$$

with ψ_k the wave function of state k of the emitter, and H the Hamiltonian governing the dynamics of the system. Essentially, this means that the elements of the transition matrix M depend upon quantum-mechanical properties of the emitter itself and of its immediate environment on the scale of wave-functions, as is discussed in [31, 32]. However, when considering optomechanical systems orders of magnitude larger in size than individual atoms, it is of more relevance to consider how the optical density of states seen by the emitter may be modified.

The optical density of states $\rho(\omega_{ij})$ describes the number of states accessible per unit volume to the emitter for transferring its excitation energy - given by ω_{ij} - to its surroundings; here, we consider i as the excited and j as the lower-energy state to which the emitter decays. For example, if an excited emitter is placed near a waveguide or inside a resonator, only certain states will be available to the emitter for radiative decay - these states are determined by the modes that can be supported by said waveguide or resonator. In general, any dielectric or metal interface placed in the vicinity of the emitter will modify its radiative decay rate to a certain extent. This happens via two

pathways: the interface modifies the boundary conditions of the electromagnetic field, thus changing the optical mode density, and also by non-radiative transfer from the emitter to the interface. Hence, by design of the nature of the interface, one can control the radiative decay rate of an emitter placed near it.

The simplest case of an interface is that of a single, planar one. For example, a perfect mirror placed near an emitter would reflect the incident radiation from said emitter, leading to interference between the incident and reflected radiation. This situation can be seen in the classical picture as that of a driven, damped dipole where the emitter, modeled by a point source dipole, is damped as it radiates energy, but is then also driven by the radiation reflected off the mirror.

The amplitude and phase of the reflected radiation determine the extent of constructive or destructive interference at the site of the emitter; this depends on the separation of the emitter and the reflecting boundary. This means that there exists a distance dependence of the optical density of states on the separation of the emitter and the reflecting interface. For separations where the interference is destructive, the density of states has a non-zero minimum as both the emitted and reflected field strength decays during propagation; this also leads to a damped oscillation of the lifetime. For constructive interference, the optical density of states is that for free space, given by $\rho(\omega) = \frac{\omega^2}{\pi^2 c^3}$ [32]. In 4a, the measured and theoretical distance dependence of the fluorescence lifetime Eu^{3+} ions near a silver mirror is shown, and the damped oscillation of the lifetime of the emitters is clearly visible for $d > 30\,nm$.

Apart from the separation of the emitting dipole to the interface, the relative orientation of the dipole to the interface also plays an important role in how the presence of the interface modifies the emitter's decay rate. This can be explained in the following picture, considering a metallic interface: a dipole oriented parallel to the interface will produce a mirrored, anti-parallel dipole which weakens the strength of the effective dipole, composed of the sum of both dipoles. On the other hand, a dipole perpendicular to the interface will produce a parallel image dipole, with the effective dipole now having ideally twice the magnitude of the original one. This is depicted in 4b:

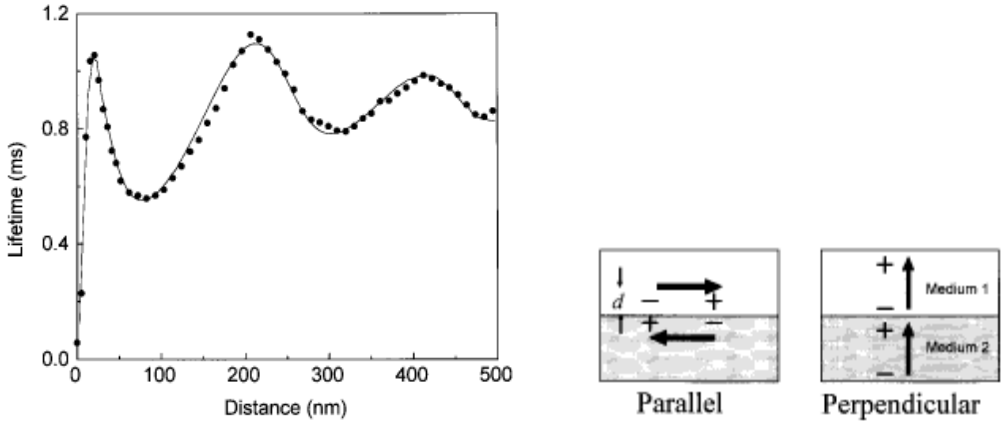

(a) (b)

Figure 4: (a) Distance dependence of lifetime of Eu^{3+} ions near placed near an Ag mirror. Plotted are measured data (dots) and a theoretical fit (solid line). For small separations below approximately 30 nm, a strong reduction of lifetime is observed, whereas for larger separations a damped oscillation of the signal with distance sets in. This matches the theory, where interference effects between emitted and reflected radiation dominate for large separations, yielding an oscillating signal similar to that in an interferogram, whereas for small separations, other non-radiative decay processes dominate. The damping of the signal for large separations is due to the point-source nature of the emitter, where the emitted and therefore also the reflected intensity is decreases with separation. In this case, the dipole orientation is free to rotate and thus samples some average orientation with respect to the mirror surface. (b) Dependence of effective dipole strength on emitting dipole orientation: the emitting dipole in Medium 1 a distance d away from the surface of Medium 2 creates an image dipole in Medium 2. If the emitting dipole is parallel to the surface (left image), the image dipole is anti-parallel, reducing the strength of the effective dipole made up of both dipoles. In the case of the emitting dipole being perpendicular to the surface, the image dipole is parallel to it, thus making the effective dipole ideally twice as strong as the emitting dipole. Images taken from [31].

The model described above is valid for emitter-interface spacings above $\lambda/4$, with λ being the emission wavelength of the emitter, and a perfectly reflecting, non-absorbing mirror as an interface in vacuum. Considering a more physically real system where there is a dielectric "spacer" medium between the emitter and the highly reflective mirror, there may be guided modes supported in the dielectric medium to which some of the emitted radiation may couple, this also being a non-radiative decay path in the sense that no free-space photon is emitted. The extent of this coupling of course depends on wave-guiding capabilities of the spacer, which in turn are highly dependent on the type of dielectric material and its surroundings. This system was studied by Drexhage [33]. From an experimental point of view, if there is air separating the emitter and the mirror,

this decay path can be neglected as there is no refractive index mismatch between the dielectric medium and its surroundings, and thus no wave-guiding possible. As will be discussed later in this work, this is the case for the experiment shown, therefore this decay path is neglected.

In the regime below separations of $\lambda/4$ - usually described as the "near field" - other decay processes also exist. These processes offer an alternative to photon emission as a decay mechanism, leading to a strong reduction of excited state lifetime - this phenomenon is thus also termed "fluorescence quenching". They are not accounted for in the description using the interference of the radiated and reflected fields. The effect is clearly visible in 4a, where for distances smaller than approximately $30\,nm$, a strong reduction of the lifetime is observed.

For an emitter and a metal-dielectric interface in the near-field regime, one non-radiative decay path is the coupling of the emitter to surface plasmon polariton (SPP) modes - this is the case for the example shown above in 4a, where the emitting ions are in close proximity to the metallic mirror. These modes arise through the coupling of an electromagnetic field with charges at the surface of the metal part of the interface. As is described in more detail in [34, 31], coupling photons to SPP modes on a metal surface in general requires some structure on the metal surface to match wave-vectors and momenta of far-field photons and SPPs. However, in the near-field, the emitted field comprises many wave-vectors which cannot propagate into the far-field, but of which some can couple to SPP modes, providing a further non-radiative decay path for small separations. However, coupling to SPP modes also requires the existence of sufficient free charge carriers on the surface of the medium. For a metal, these are readily available, but other materials such as semiconductors may require a certain amount of electron doping to support SPP modes.

The last decay mechanism to be discussed here is non-radiative resonant energy transfer from the emitting dipole to dipoles in the interface material. The classical theory of this is based on the principle of Förster resonant energy transfer (FRET) [35], which has come to be associated with the transfer of energy between resonant dipoles of molecules in close proximity, typically 2-6 nm [36]. The emitting dipole field is modeled as its near field, yielding a distance dependence of the strength of the energy transfer process proportional to d^{-3}, where d is the spatial separation of the donor and acceptor dipoles. This is observed as a distance dependence of the fluorescence lifetime decay rate. Persson et al. [37] provide a rigorous derivation for dipole resonance between a single emitting dipole and dipoles in a surface or bulk material, yielding a distance dependence proportional to d^{-4} and d^{-3}, respectively.

Graphene, being atomically thin and displaying electronic properties similar to those

of a 2D electron gas make it an ideal candidate for studies of resonant energy transfer between a surface and a radiating emitter. Theoretical studies for the quenching behaviour of different emitters placed near graphene have been performed, for example for dye molecules by Swathi et al. [20]. In this study, an expression for the distance dependence of the rate of electronic excitation energy transfer from the dye molecule to the graphene sheet is derived, predicting a strong distance dependence of the form $R \propto \frac{e^{-bd}}{d}$, with R being the energy transfer rate, d the distance and $b = \frac{2\Delta E}{t\sqrt{3a}}$ is a constant where ΔE is the energy difference between the ground and excited vibronic levels of the dye molecule, a is distance between atoms along one lattice vector in the graphene lattice, and t is the nearest neighbour matrix element. This distance dependence of decay rate was found to be valid in the short range for separations in the range up to $20\,\mathring{A}$, in which resonant energy transfer is the predominant decay path.

However, in a subsequent study [21], the distance dependence was found to have a d^{-4} dependence for pyrene. This corresponds to the dependence found for metals as discussed previously. Furthermore, this additional study suggests that distance dependence should be visible up to a separation range of $30\,nm$, at which distance the natural decay lifetime and the modified lifetime due to the graphene coincide for the pyrene molecule considered. This is important when considering an experimental verification of this theory, as extremely small separations in the range of Ångstroms are harder to control compared to separations on the nanometer scale.

In an extension to this first theoretical approach to lifetime quenching with graphene, Gómez-Santos and Stauber [16] include transverse dipole moments of graphene compared to the solely longitudinal approach of Swathi et al. - this means that both in-plane and out-of-plane excitations of the dipoles in graphene are considered. The calculations also include a photon propagator instead of assuming an instantaneous energy transfer, and the case of doped graphene is also considered. In their approach, the decay of a fluorescent atom is split into a radiative and non-radiative part, γ_r and γ_{nr} respectively, the total decay rate being given by $\gamma = \gamma_r + \gamma_{nr} + \gamma_{abs}$, with γ_{abs} the decay due to absorption by the graphene itself. However, when considering the rate of radiative and non-radiative energy transfer, the absorption by graphene is negligible. The rate of observed photons (fluorescence) at a distance z from the graphene is given by $\Phi(z)$. The ratio of observed fluorescence at a distance z, $\Phi(z)$, compared to that at infinite distance Φ_∞ can then be written as:

$$\frac{\Phi(z)}{\Phi_\infty} = \left(1 + \frac{\gamma_{nr}}{\gamma_r}\right)^{-1}$$

Here, the ratio $\frac{\gamma_{nr}}{\gamma_r}$ can be approximated by $\frac{\gamma_{nr}}{\gamma_0}$, where γ_0 is the vacuum decay rate, as graphene modifies the radiative decay rate only by a very small amount on the order of α. This approximation yields three terms in the result for the ratio after some calculation, details of which are to be found in [16]:

$$\frac{\gamma_{nr}}{\gamma_r} \approxeq \frac{\gamma_{nr}}{\gamma_0} = a\tilde{\gamma}_1 + b\tilde{\gamma}_2 + c\tilde{\gamma}_3$$

These three contributions have pre-factors a, b, c to account for the possible geometrical dipole orientations perpendicular to and in the graphene plane, some constants as well such as the fine structure constant α as well as other functions that are approximately $= 1$. The first term, $\tilde{\gamma}_1 \propto \left(\frac{\lambda}{z}\right)^4$ corresponds to the longitudinal excitation of graphene, as found by Swathi et al. previously. The second and third terms $\tilde{\gamma}_2, \tilde{\gamma}_3 \propto \left(\frac{\lambda}{z}\right)^2$ correspond to uncharged, transverse excitations of graphene that were previously not considered and dominate at longer distances in the regime $\frac{z}{\lambda} > 0.2$. However, the first and originally established term still dominates in the range $0 < \frac{z}{\lambda} \lessapprox 0.2$, which for visible wavelengths such as e.g. $\lambda = 630$ nm yields $z_{max} \approxeq 130$ nm as a threshold distance for the inverse fourth power law dependence. The distance dependence is shown in 5. It is noteworthy that all terms in the ratio $\frac{\gamma_{nr}}{\gamma_r}$ are only dependent on z, λ and α (contained in the prefactors of $\tilde{\gamma}_i$), which means that by measuring fluorescence quenching, one can extract very precise measurements of distance of a graphene sheet to the emitter independent of the material used.

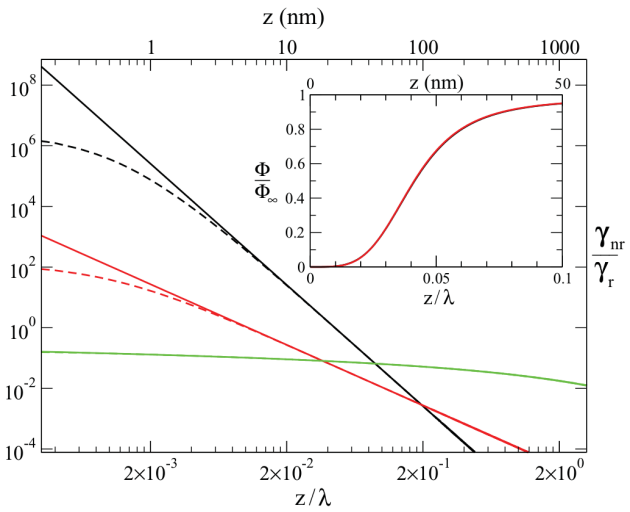

Figure 5: Distance dependence of non-radiative to radiative decay rate $\frac{\gamma_{nr}}{\gamma_r}$. Solid lines represent the analytical result for the components $\tilde{\gamma}_1$ (black), $\tilde{\gamma}_2$ (red) and $\tilde{\gamma}_3$ (green). The corresponding dashed lines represent the exact terms. Inset: distance dependence of normalized fluorescence $\frac{\Phi(z)}{\Phi_\infty}$ (see text) to normalized distance $\frac{z}{\lambda}$, with $\lambda = 500\,nm$. Source: [16]

The effect of doping on graphene's ability to quench fluorescence is also discussed in [16]. The range of frequencies ω in which plasmons may be excited in graphene through interband transitions is defined by $\hbar\omega \lesssim 2\,E_F$ [38], with $\hbar$ the reduced Planck's constant and E_F the Fermi energy. For visible wavelengths, $\hbar\omega \approxeq$1 - 3 eV, which means that the Fermi level of graphene should be $E_F \approxeq$0.5 - 1.5 eV, requiring a high level of doping, if one considers $E_F \approxeq$ 0.1-0.2 eV for a typical graphene device on a silicon dioxide substrate. However, if this inequality is fulfilled by sufficiently high doping or sufficiently low-energy photons, coupling to plasmons in graphene is possible and has been shown experimentally [39]. Then, the distance dependence of the decay rate becomes exponential: $\frac{\gamma_t}{\gamma_0} \propto e^{-z/z_0}$ [20], where γ_t is the decay rate due to plasmon mode coupling, and z_0 is a characteristic length scale. For graphene with no or very low levels of doping at visible incident wavelengths it is therefore not possible to excite plasmon modes, which means that this non-radiative decay path must not be taken into account in the framework of the experiment described in this thesis. In summary, the original model of an inverse fourth-power distance dependence of the decay rate due to resonance energy transfer is the most appropriate approach.

2.2 The Mechanical Properties of Graphene Membranes

2.2.1 Elastic Properties

As for its optoelectronic properties, graphene's mechanical properties are also a direct result of its lattice structure, where the strong inter-atomic bonds between the carbon atoms play a defining role. Various experimental studies have shown that Young's modulus of graphene is on the order of 1 TPa, and its Poisson ration $\nu \approxeq 0.16$ - 0.18. Young's modulus is the ratio of tensile stress to tensile strain in the regime where Hooke's law is valid, and is used to characterize the stiffness of elastic materials, while Poisson's ratio is the ratio of transverse to axial strain along the axis of the load applied. As such, graphene is one of the strongest materials on earth - for example, it is approximately 6 times stiffer than steel [40]. This is remarkable given its atomic thickness.

To measure these properties, a common technique is to use an atomic force microscope (AFM) tip to apply a controlled force to a suspended graphene sheet while measuring its deflection when in contact [11, 14]. In a different approach, graphene's impermeability to gases is used to bend membranes by a pressure gradient across them while simultaneously measuring their resonance frequency. This approach has the additional benefit that it allowed the first measurement of the mass per area of few layer graphene, yielding $m \approxeq 3\,\mu g\,m^{-2}$ [41].

2.2.2 Nanodrums and the Thin Plate Model

For nanomechanical systems, the exploitation of graphene's unique properties to make nanomechanical resonators is of large interest as previously unreachable quality factors and high resonance frequencies are achievable. These nanoresonators can be used for a wide range of applications ranging from ultrasensitive mass sensors, distance measurement at the quantum fluctuation limit and as an experimental platform to investigate back-action cooling [13]. In this thesis, the main focus shall be on what is commonly referred to as a "drum structure" - a circular hole in a substrate, covered by a graphene sheet to form a clamped, circular membrane.

To predict the properties of this drum structure under loading by an applied electric field, a thin plate capacitor model is used; this is conceptually justified considering graphene as an atomic monolayer. Nonetheless, it is important to note that while graphene may be atomically thin, this does not necessarily imply that it is totally flat. This is also true for suspended membranes, which may have wrinkles and may become more wrinkled upon loading, as is discussed in [42]. However, experimental studies have

been performed by Wong et al., where suspended graphene membranes were loaded by applying an electrostatic force and the results were compared to thin plate theory, showing good agreement [12].

The thin plate model is used to predict the maximum central deflection d_0 of the circular membrane. This is given as:

$$d_0 = \frac{P\,a^4}{64\,D} \tag{3}$$

where P is the uniform loading of the plate, i.e. the force per area applied uniformly across the surface of the plate, a is the plate radius and D is the flexural rigidity - the force required to bend a given flat sheet to unit curvature. It is defined as:

$$D = \frac{E\,h^3}{12\,(1-\nu^2)}$$

with h the thickness of the sheet, E Young's modulus and ν the Poisson ratio of the material. Under the assumption that the shape of the drum does not change for the deflection regime considered, one can assume the deflection d at a given radius r in the area of the drum to be:

$$d = d_0\,(1 - \frac{r^2}{a^2})$$

This assumption is valid for membranes where the maximum deflection $d_{0,max} \ll a$. Wong et al. use an approach where the strain of the membrane is included for deflections larger than the drum thickness, which is a regime easily accessed when considering atomically thin graphene membranes. This approach results in the following implicit expression for the maximum central deflection d_0:

$$d_0 = \frac{P\,a^4}{64\,D}\,\frac{1}{1+(\frac{0.4418}{1-\nu^2}\,\frac{d_0^2}{h^2})} = \frac{P\,a^4}{64\,D}\,\frac{1}{1+0.455\,\frac{d_0^2}{h^2}} \tag{4}$$

In Eq. 4, one can see that there is an additional term on the right hand side of the equation compared to the original thin plate equation Eq. 3. This accounts for the strain of the central part of the membrane when $d_0 \gg h$, with $\gg$ implying at least a few times larger.

2.2.3 Electrostatic Deflection of Graphene Membranes

Considering equation Eq. 4 for the central maximum deflection, it is now of interest to consider the case for a single layer graphene membrane loaded uniformly over its area

by an electrostatic force. The situation is depicted in Fig. 6:

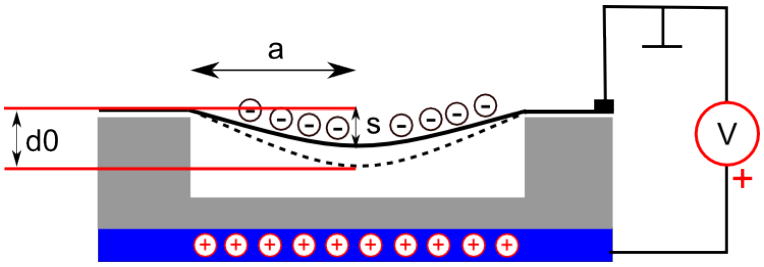

Figure 6: Illustration of electrostatic deflection model for a thin graphene membrane (black solid line) of radius a suspended over a hole in a dielectric material (grey area): an external voltage is applied, with the positive terminal applied to an electrode (blue), causing the grounded membrane to be electrostatically attracted towards it. Before deflection, the membrane has some initial sag s, upon loading by the electrostatic force its maximum central deflection is at d_0 (dashed line).

The loading P, or force F per area A applied to the membrane by application of a voltage V between the membrane (anode) and a backgate electrode (cathode) at some distance away is given by:

$$P = \frac{F}{A} = \frac{\epsilon_0 \, \epsilon_r \, V^2}{2 \, (s - d_0)^2}$$

Here, s is the sag of the membrane, i.e. its central deflection without any applied voltage. This must be included as any real membrane not perfectly taut over its area will feature some initial displacement compared to its clamped edges. For graphene membranes, this can happen when the area of the graphene forming the membrane is slightly larger than the surface area of the hole over which it is suspended. When considering the effective permittivity ϵ_r of the dielectric material between the membrane and the cathode, one must take into account all layers of materials separating them. This gives rise to a compound effective permittivity of the following form:

$$\epsilon_r = \frac{\sum \epsilon_i t_i}{\sum t_i}$$

where ϵ_i is the effective permittivity of an individual layer, and t_i is its thickness. The result of this analytical model is shown in Fig. 7, where the backgate voltage dependence of d_0 is shown for various membrane diameters. As expected, the amount of deflection for a given backgate voltage scales with membrane diameter. The hole model used here is a layered one, based on the sample design discussed later in Section 3.4. The hole bottom made of 165 nm SiO_2 substrate, covered by 30 nm PbS quantum

dots and 7 nm SiO_2 capping layer on top. This layer structure is taken into account for the compound effective permittivity, and experimentally determined sag values are used for each hole diameter.

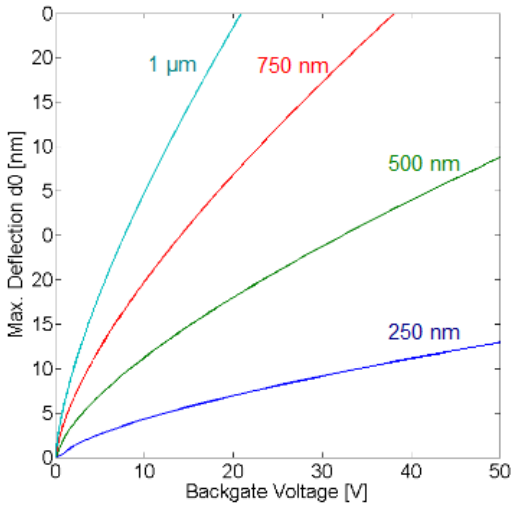

Figure 7: Analytically calculated maximum central deflection d_0 of a single layer graphene membrane of thickness h =0.34 nm, suspended over a hole of depth 120 nm with varying diameters from 250 nm to 1 μm. The hole is simulated to consist of a bottom layer of SiO_2, followed by 30 nm of PbS quantum dots covered with 7 nm of SiO_2 capping layer. The initial sag is adjusted for each hole diameter. It is clear that the diameter of the membrane has a significant effect on how each membrane deflects, the amount of deflection being proportional to it for a given backgate voltage.

2.3 Quantum Dots

Semiconductor nanocrystals are low-dimensional structures at the nanoscale consisting of one or more types of semiconducting material. Despite usually having dimensions significantly larger than a single atom, they can display quantum confinement properties and may be considered as multidimensional quantum wells, depending on their geometry. In the context of this thesis, the main focus shall be on their optoelectronic properties, in particular those of quantum dots.

Quantum dots are particles with diameters on the order of nanometers, consisting of one or more shells of various materials such as cadmium selenide (CdSe) or lead sulfide (PbS). They confine charges in three dimensions and can thus be considered as 3D quantum wells, with the associated energy spectrum. The degree of confinement depends on the size of the quantum dot relative to the exciton Bohr radius. This radius describes the separation of the excited electron-hole pair that form the exciton, and is

derived from the distance between the proton and electron in a hydrogen atom. Strong confinement is achieved when the exciton Bohr radius is smaller than the quantum dot radius [43]. In this case, the dimension of the quantum dot strongly influences its energy level structure and therefore also its optoelectronic properties such as the fluorescence emission peak. Electron-hole pairs (excitons) can be excited when a quantum dot absorbs an incident photon of sufficient energy, promoting an electron to a higher-energy state from the ground state in the quantum well. Once created, the exciton is then trapped in the structure and can be modeled as an oscillating dipole with random orientation, associated with a certain excited state lifetime after which the electron and hole recombine.

For quantum dots, various recombination mechanisms that can be subdivided into radiative and non-radiative processes exist. The local environment of the quantum dot has a strong influence on the dominating decay process. For example, a single, isolated quantum dot may only relax radiatively, whereas a quantum dot in a cluster can exchange energy or charges with its neighbours, increasing the probability of non-radiative decay such as FRET or charge transfer.

During the quantum dot fabrication process, long-chained organic ligands are attached to the quantum dot surface. Their length determines the proximity of individual quantum dots in a cluster. Furthermore, the ligands may passivate electron traps on the quantum dot surface thus increasing the excited state lifetime by trapping free electrons, which inhibits exciton recombination. The extent to which charge transfer is possible and with it the electrical conductivity of quantum dot films strongly depends on the ligand length. An example of a long ligand is oleic acid with 15 carbon atoms along its chain, which leads to low film conductivity but is still short enough for FRET to occur between quantum dots. For closely-packed clusters, the energy levels in an individual quantum dot may also change due to close proximity to another, causing the formation of a double quantum well with altered electronic states. Clustering can also lead to broadening of the fluorescence spectrum, as is shown in [44].

For the work done in this thesis, colloidal PbS quantum dots fabricated by a hot injection method similar to that described by Hines et al. [45] were used. They consist of nanocrystals approximately 1-2 nm in diameter with oleic acid ligands, dissolved in toluene at a concentration of 5 mg / mL. The absorption peak lies at approximately 550 nm. As discussed above, the oleic acid ligand makes films of PbS quantum dots have a very high resistance, thus the predominant energy exchange mechanism between the quantum dots in a film is FRET, leading to a change in excited state lifetime compared to that of an individual quantum dot. However, for measurements of lifetimes of the film, an equilibrium between FRET to and from each quantum dot is assumed, leading

to an ensemble lifetime which can be measured. As the quantum dots used here had a size distribution of only approx 5 % around their nominal size, the fluorescence spectrum of these films is expected to be only slightly broader than that of an individual quantum dot. The measured spectrum of a film is shown in Fig. 8, with its excitonic peak at 726 nm. This corresponds to spectra shown in the literature [44].

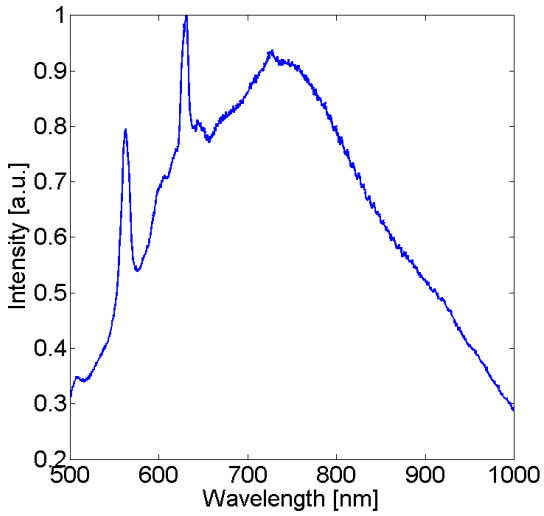

Figure 8: Fluorescence spectrum of PbS quantum dots with the excitonic peak at 726 nm. The two peaks at 560 nm and 630 nm are caused by ambient lighting, and are not part of the actual emission spectrum.

The degradation of quantum dot films when exposed to oxygen and high temperature strongly influences the intensity of fluorescence emission, and can also change the emission peak [46, 47]. For the work presented here, the emission intensity is critical as it determines the signal-to-noise ratio in photoluminescence images and fluorescence lifetime measurements (see Sections 3.2 and 3.3). Atmospheric oxygen causes the oxidation of the outer shell of the quantum dot, making its semiconductor core become effectively smaller compared to its total size, thus inducing a blue shift in the emission. The more detrimental effect with regard to this work is that oxidation can also strongly and irreversibly reduce the emission intensity for a given excitation wavelength as the number of surface traps and the bandgap energy increases with respect to the unoxidised quantum dot. The process of the decrease of emission intensity is commonly referred to as "bleaching".

To reduce the effect of oxidation for samples coated with thin films, two possible solutions are storing and measuring the sample in nitrogen or vacuum, or coating it with a protective capping layer. In nitrogen or vacuum, trapped oxygen may disperse out of the sample again, thus increasing the photoluminescence. Thin capping layers

can be deposited on quantum dot films by atomic layer deposition or evaporation; this has been shown to protect them from oxidation [48]. For the work presented here, it is important that any capping material considered should be transparent to both the excitation and emission wavelength, and the deposition process should not damage the quantum dot layer. The coating process used is described in Section 3.4.

3 Measurement Techniques and Experimental Setup

3.1 Atomic Force Microscopy

One of the most popular and reliable methods to measure the topography of surfaces on the nanometer scale is atomic force microscopy, invented in 1986 by Binnig, Quate and Gerber [49]. Its measurement principle relies on the deflection of a cantilever with a microscopic tip in close proximity to a surface, this deflection being measured as the tip is scanned across the sample surface. The deflection of the tip is caused by the one or more forces acting on it, originating from the surface being scanned. Some examples of common forces causing cantilever deflection are electrostatic, van der Waals, magnetic and mechanical forces. With modern atomic force microscopes (AFMs), it is even possible to pass current through or to heat the tip, allowing a large variety of sample properties to be measured with very high horizontal and vertical precision. Giessibl [50] provides an extensive summary of available AFM techniques and their uses.

The deflection of the tip is measured by focusing a laser onto the cantilever and detecting its movement using a four-quadrant photodiode. The sample to be scanned is mounted onto a piezoelectric stage, and a feedback loop is used to control the distance between the tip and the sample surface. This control loop is set to keep the distance between the tip and the sample surface constant, thus avoiding collisions with the surface that can break the tip. A map of the voltage that must be applied to the piezoelectric stage to keep the distance constant thus yields the topology of the sample. During the scanning of the sample, the tip may be in direct contact with the surface ("contact mode") or may also be set to oscillate very close to the surface ("tapping mode").

In contact mode, stiff tips are used that are in direct contact with the surface, thus providing a noise-free image even for samples covered in liquids. It requires samples with relatively hard surfaces, and was the first used to see individual atoms on a surface. Furthermore, contact mode was used to find the elastic properties of graphene membranes by actively deflecting them with a known force and measuring the tip displacement, as described in [14].

The use of tapping mode is advantageous for delicate samples (e.g. biological cells) and requires the cantilever to oscillate at its resonance frequency, which must be measured accurately before scanning the sample. While being scanned across the sample, the tip never actually touches the surface, but the surface forces acting on it change its resonance frequency. In this case, the feedback loop is used to keep the resonance frequency constant. This mode has the advantage that the phase of the cantilever pro-

vides additional information about the material type under the tip, thus tip oscillation phase changes can be used to accurately determine the location of material interfaces.

(a) (b)

Figure 9: (a) Silicon AFM tip with nominal 8 nm tip radius. (b) AFM cantilever with the tip shown in (a). Source [51]

For all the AFM measurements done as part of the present work, a *Veeco Dimension 3100* AFM was used in tapping mode. In this mode, sample surfaces and suspended graphene membranes were imaged so as to minimize the possible damage to the membranes and to be able to use the phase information to determine the location of the graphene on the sample. A typical silicon tip is shown in Fig. 9a, together with the cantilever it is mounted on (see Fig. 9b). These tips have measured resonance frequencies in the range of 350 - 400 kHz and spring constants of 20 - 80 $N\,m^{-1}$. Using these tips, scanning speeds of approximately 40 $\mu m\,s^{-1}$ for up to 35 μm scan lengths could be reached with 384 lines per sample, thus allowing a relatively large area of the sample to be scanned while still achieving a resolution high enough to show details. A typical image of a sample with a hole array structure partially covered with a graphene flake on the right is shown in Fig. 10a, together with the corresponding phase map Fig. 10b. From these images, one can see how the topological and phase information can be complementary: while the hole and surface structure is clearly visible in the topography, the graphene flake edge is more clearly visible in the phase map.

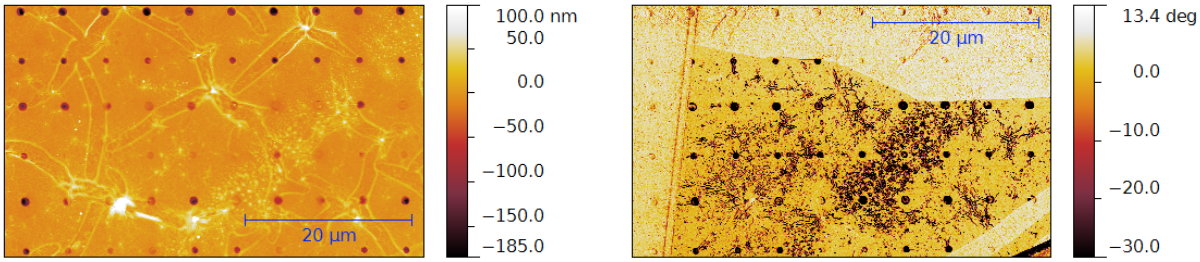

(a) (b)

Figure 10: Typical false-colour AFM image of a hole array structure partially covered by a graphene flake on the right. Shown are (a) the topography and (b) the phase information, both acquired in tapping mode. It can be seen that the two images are complementary in their information, with the topology information showing clearly the partially covered holes and their depth, whereas the phase shows more precisely the edges and location of the graphene flake.

To measure the degree of deflection of a graphene under electrostatic loading, a backgate voltage was applied to the sample while scanning it with the AFM. However, it was observed that this led to very fuzzy images above voltages of approximately 2 V. This was attributed to a charging of the AFM tip while scanning, causing it to deflect much more than the deflection induced by the sample. To resolve this, a platinum-coated tip was used that was electrically grounded to allow it to discharge, producing sharp images of the deflected membranes.

3.2 Scanning Photoluminescence Measurement

To obtain 2D maps of photoluminescence of the devices fabricated, the setup shown in Fig. 11 was used. The excitation source can be chosen to be a continuous wave (CW, Laser Quantum ventus model) or pulsed laser (PicoQuant LDH-P laser head with PDL 800-D driver), both emitting at 532 nm. The pulsed laser has a pulse duration of 70 ps and a variable repetition rate from 31.25 kHz to 80 MHz. After source selection, the emitted beam is expanded and spatially filtered to obtain a beam with a clean, Gaussian intensity profile. The beam is then passed through one of a set of neutral density filters, allowing for quick and simple attenuation of the beam, e.g. for alignment. The attenuated beam is then reflected off a dichroic mirror, into a set of two perpendicular galvanic mirrors. These can control the beam's direction in the vertical and horizontal direction, and are computer-controlled. A set of two irises can be closed to form pinholes for the alignment of the beam, but are left open during operation so

as not to block the beam path. Finally, a high numerical aperture objective (Edmund Optics 59880, 100x magnification, NA = 0.8) focuses the light onto the sample, held in a sample holder.

The photoluminescence (PL) signal from the sample is then collected in the same objective, and takes the same path as the excitation beam until it is transmitted through the dichroic mirror. The PL signal is then filtered optically by a combination of a notch filter at 532 nm and a low-pass filter at 561 nm to remove unwanted excitation radiation and other high-frequency radiation, respectively. Finally, the remaining signal is incident on an single photon avalanche photodiode (APD, Micro Photon Devices PDM series) which converts a single incident photon to a TTL pulse.

To select the area of interest on the sample, a fibre white light source can be flipped into the beam path and the image of the sample is reflected onto a CCD camera via a beam splitter which is also flipped into the beam path. The sample holder, mounted onto a micrometer stage, can be moved in the plane of the sample using two micrometer screws. For inital focusing of the laser spot and alignment, the camera can also be used without the white light source, together with a third micrometer screw that moves the sample holder along the direction of the beam.

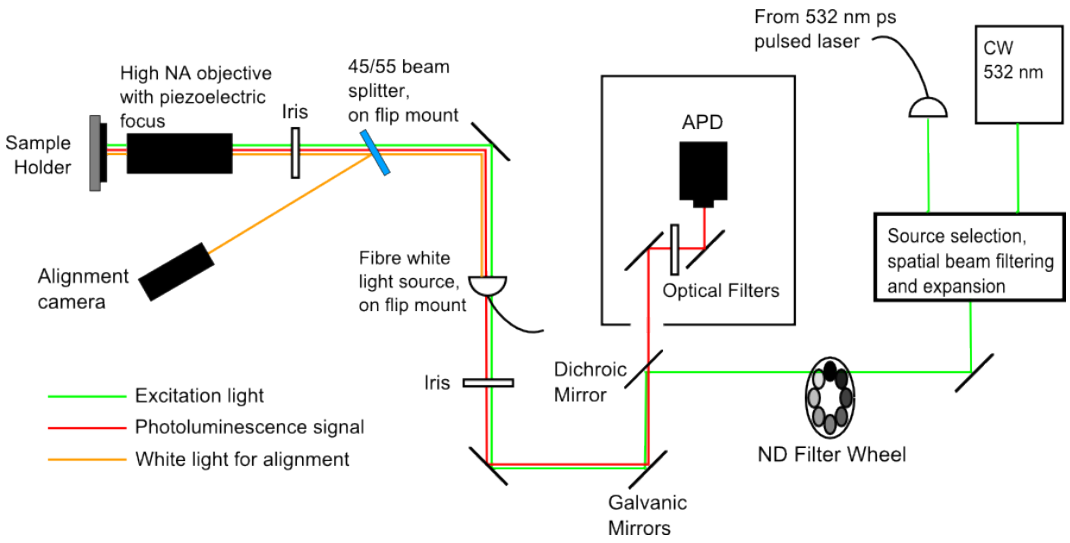

Figure 11: Optical setup used to scan the fluorescence signal from the sample: a CW or pulsed laser source can be selected as the excitation source; its beam (green line) is then expanded to fill the back-aperture of the objective (not all optical elements are shown here). Using various ND filters selectable on a filter wheel, the laser radiation intensity can be controlled. The attenuated beam is then reflected by a dichroic mirror, followed by two perpendicular galvanic mirrors which control the beam direction. The directed beam then passes through two irises that can be closed to form pinholes for alignment. Finally, the excitation beam is focused onto the sample by a high NA objective with a piezoeletric focusing unit. The PL signal from the sample is collected by the same objective, and takes the same path back as the excitation beam up until the dichroic mirror, which is transparent for the longer-wavelength PL signal. This passes thourgh the dichroic mirror, and is then filtered again to remove residual components of the excitation wavelength (532 nm notch filter) and shorter-wavelength components (561 nm low-pass filter). Finally, this filtered signal is then collected and converted to an electric signal by an APD. Additionally, the setup features an alignment camera and a whilte light source that can be flipped into the beam path. This can then be used to move the sample in its holder to locate the area of interest before scanning.

To perform a 2D scan of the photoluminescence of a sample, the following steps are taken: first, the laser power is measured using a power meter with its photodiode placed directly in front of the objective, and adjusted to the desired value. Then, the area of interest on the sample is found using the camera and the white light source. The laser source is then focused manually, still using the camera but with the white light source flipped out of the beam path. This is done in an area slightly outside the area of interest to prevent a premature bleaching of the photoluminescence there, and with attenuation of the laser to prevent damage to the camera. Using a Python control environment, the galvanic mirror orientation is changed to move the laser to different spots, which are marked on the optical image. This is done to provide a reference for

the scan area - an example of this is shown in Fig. 12a, where the blue crosses are selected positions of the laser spot for different galvanic mirror orientations, overlayed onto the optical image seen by the camera at that location. Using this reference, the area to be scanned can easily be identified and adjusted by moving the sample holder in the sample plane.

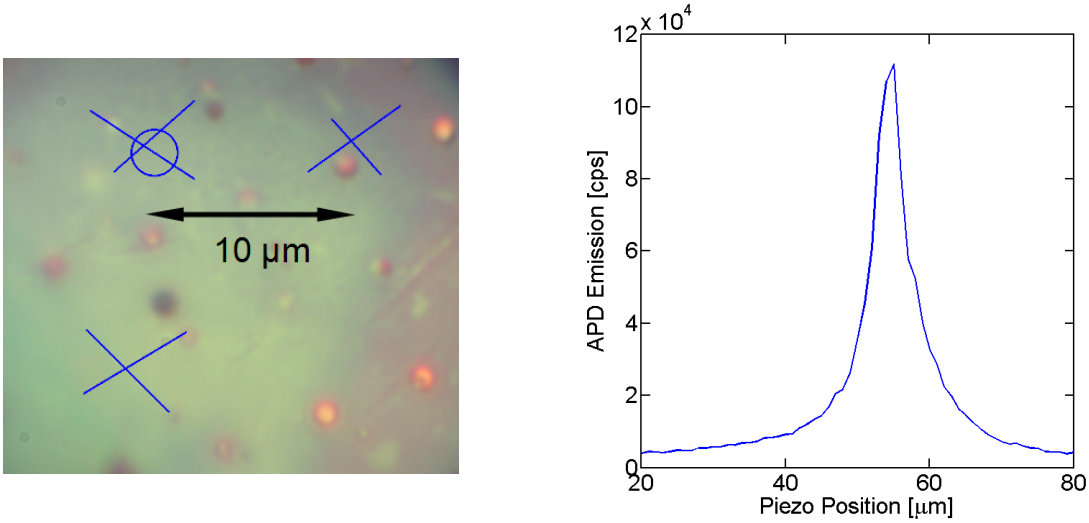

(a) (b)

Figure 12: (a) Overlay of reference laser points (crosses) and camera image in PL setup. A part of the graphene flake to be scanned is visible in the background, but not focused as the focus is optimized for minimum laser spot size in this image. (b) APD counts vs. piezo position during focusing.

Once the sample is at the correct position with respect to the laser, the beam splitter is removed from the beam path, and the laser is fine focused, at a location just outside the area of interest to prevent bleaching. The focusing is done by using a Python script that moves the objective along the direction of the beam path with a piezo micro-positioner, and simultaneously records the number of counts recorded by the APD. The piezo is then set to the position where the maximum number of counts was recorded; an example of this focus scan shown in Fig. 12b. It is necessary to perform a focus scan before each measurement to ensure a good quality of the PL image, as even small movements of the sample will lead to blurred images.

At this point, the system is ready to scan the sample. This is done using a Python script again, its input parameters being the scan size in the x and y directions in the sample plane, and the number of points to be recorded per direction, as well as the integration time per point, during which the number of counts from the APD is

averaged.

The scan resolution is given by the diffraction limit: $r_{diff} = \frac{0.61\,\lambda_{fl}}{NA} \approxeq 550$ nm for a fluorescent emission wavelength $\lambda_{fl} \approx 730\,\text{nm}$ for PbS quantum dots. However, if the emitter being scanned has a non-linear response to the excitation intensity, a better resolution may be achieved. This is because fluorescence only occurs above a certain excitation intensity, if this threshold is above the full width at half maximum, the resolution is higher than that in the diffraction limit.

3.3 Measurement of Emitter Excited State Lifetime

To measure the excited state lifetime of an emitter using a sampling approach, one would have to sample the intensity of the radiating emitter after excitation at a sufficiently high sampling rate to be able to reconstruct the decay trace. Using a physical model of the emitter that provides a definition of the lifetime, one can then extract this from the measured data. Here, a technical problem arises due to the fact that typical fast decay times are much too short to be able to measure them directly with an analogue sampling technique, where an analogue measure of the emission is performed at certain times defined by the sampling rate. For example, an emitter with a short lifetime may decay in 200 ps - if 10-15 data points want to be sampled in this time for reconstruction, a sample must be taken every 10-20 ps. This implies a sampling rate in the range of GHz, which is not technically feasible with current readout electronics. The extent of this limitation depends on the combination of the type of emitter to be studied and the signal detection and processing that is used, making measurements possible for extremely slowly decaying emitters.

However, a more serious issue is that for many emitters, the photoluminescence signal is very weak, and may only consist of few or even single photons in a given sampling period, making it near impossible to sample in an analogue manner as described. For this reason, Time-Correlated Single Photon Counting (TCSPC) is used to measure weakly fluorescing emitters with fast decay times. This technique employs a pulsed excitation laser that is synchronized with the readout device which measures the time between the the excitation pulse and the arrival of a photon, this measurement has a resolution of 60 ps for the APD used. Furthermore, the readout device groups the arrival times into bins, so that photons arriving within a certain time range are grouped together into one bin. This is shown in Fig. 13a:

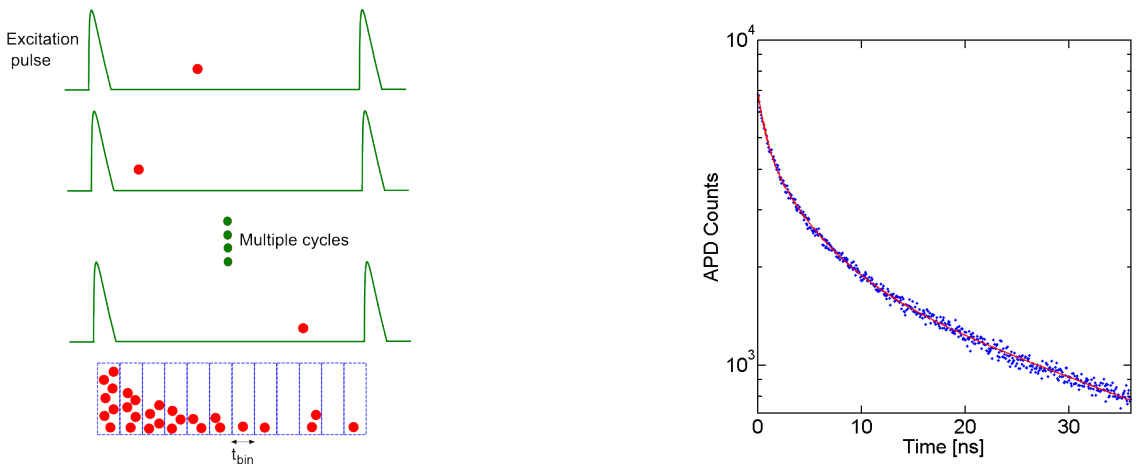

(a) (b)

Figure 13: (a) Time-Correlated Single Photon Counting: after an excitation pulse, one or more photons arrive at different times during each cycle. Photon arrival times are grouped together so that photons arriving within the same bin time t_{bin} are grouped together (blue dashed rectangles), yielding a histogram of arrival times (b) Typical histogram of photon arrival times.

A typical histogram measured with the TCSPC method is shown in Fig. 13b. This was obtained using the same experimental setup as described in Section 3.2, with the pulsed laser source selected and a PicoHarp TCSPC system to collect the APD counts. To record a histogram, the laser is set to emit with repetition rate where the time between excitation pulses is significantly longer than the longest expected emitter lifetime, so that sufficient data points are taken to be able to fit all lifetimes from the recorded data. Using the same method as for photoluminescence measurements, the sample area of interest is found and the galvanic mirrors are set to aim the beam at the point on the sample where the fluorescence lifetime is to be measured.

For the measurement, the integration time is set to a value where a sufficient number of counts is obtained to provide a good signal-to-noise level for a given number of dark counts of the APD. The integration time is the time during which the data for the histogram is collected, typically 1-10 s depending on the laser power used. The readout resolution must also be set to a value where there are sufficient sampling points but not too much noise. In general, the sampling rate limits the bandwith of noise sampled, so a lower resolution is desirable for some measurements with high-frequency noise. Finally, the time offset between the excitation pulse and the start of the photon counting module must also be set to a value where the largest possible part of the decay is observed.

An example of a histogram obtained in this way is given in Fig. 13b. With this setup it is also possible to perform 2D scans of lifetime, where a histogram is recorded

for each point in a specified area, similar to the process of making a PL map. However, to visualize this essentially 4D data (position, time and counts), it is necessary to fit the histograms and extract a lifetime at each position, which can then be plotted as a false colour map.

The background noise or "dark counts" of the APD is an important parameter that must be measured to be able to fit a given recorded histogram. This is especially true when the longest lifetime of the emitter is longer than the time between excitation pulses, so that the measured signal is still decaying when the next excitation pulse arrives. To measure dark counts, a histogram is recorded with identical settings of integration time and resolution as for the actual histogram, but with an optically absorbing material blocking the path of the excitation beam to the sample. This typically yields values of 2-10 counts, which means that the histogram measurement has low noise, given that a typical histogram is recorded with count maxima of 500 cps and above, and does not decay to the noise floor inside the excitation pulse separation time.

3.4 Sample Fabrication

During this thesis, different samples were designed and fabricated with various graphene membrane shapes, sizes and supporting structures. For the design, various parameters had to be taken into account to make it possible to deflect graphene in a separation range where fluorescence quenching is to be expected without having to apply excessively high voltages above 50 V that can cause electrical damage to the sample.

Design and Fabrication of Substrate Structure

In the first stage of design, the depth of the graphene membrane support structure had to be made such that its initial distance to the quantum dot film surface was inside a range of 20-60 nm. This separation range was chosen to probe distances of 0-60 nm, assuming the membrane would be deflected by 20 nm at most. The selected range is based on the model by Wong et al., which predicts that circular membranes of diameters 750 nm and 1 μm can be deflected by more than 20 nm in a backgate voltage range of 0-50 V (see Fig. 7). Therefore, three depths were required to cover said separation range for a given hole diameter. To determine the actual depth required to achieve the separations discussed above, the initial sag of the membrane and the quantum dot and capping layer heights and profiles had to be taken into account. These were measured using AFM scans made on test samples, as is discussed in Section 4.1.

Using the test sample data, hole and trench structures were made in silicon dioxide layers on doped silicon wafers cut into squares of 5 mm side length. Theses wafers are

specially manufactured for graphene processing, as their 285 nm oxide coating makes graphene on its surface visible due to optical interference effects [52]. Using focused ion beam (FIB) milling, holes and trenches of different depths were made in the silicon dioxide layer (see [53]). This technique was chosen to make the structures due to its superior resolution and controllability compared to other process such as optical lithography, for example. To determine the dependence of the structure depth on the ion flux dose used in the FIB, topology scans of test samples made at different doses using the AFM. This allowed the prediction of the dose to be used for a desired hole depth. The relationship is shown in Fig. 14:

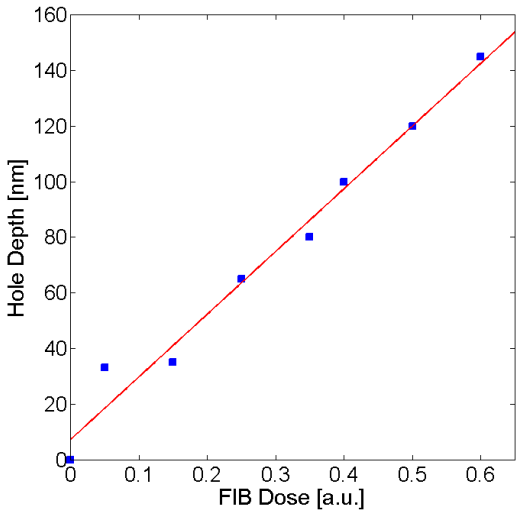

Figure 14: Measured (blue squares) and fitted (red line) hole depth vs. FIB ion flux.

Sample Cleaning and Quantum Dot Spincoating

Upon milling of the hole and trench structures, the samples were cleaned with toluene followed by isopropanol for 5 minutes each in a sonicator. Toluene was chosen as a solvent as it also dissolves remnants of quantum dot layers on the samples, which was important for samples that were being re-used after having previously been coated with quantum dots. Isopropanol removes organic residues including those remaining after cleaning with toluene. The samples were not cleaned with oxygen plasma as this was found to reduce the quantum dot film quality. This is attributed to toluene being a non-polar solvent, whereas oxygen plasma cleaning slightly polarizes the surface, decreasing the adhesion between a non-polar solvent and the substrate.

After cleaning, the samples were spun-cast with quantum dots dissolved in toluene at a concentration of 5 mg / mL. This concentration was found to produce homogeneous films of quantum dots while still being high enough. Beforehand, higher concentrations

had been used, resulting in rough surfaces and local piling of the quantum dots around edges. For samples with holes, this caused the formation of crater-like structures, as shown in Fig. 15a, whereas the surface was smoother for lower concentrations (see Fig. 15b). Before being placed on the sample, the quantum dot solution was sonicated for 5 minutes to mix it thoroughly, and a syringe with a filter with pore size 200 nm was used to put a single drop of solution on the sample, the filter preventing any remaining clusters of quantum dots to be spun-cast. To make films of approximately 20 nm thickness, the drop of quantum dot solution was placed on the sample and left for 30 s to allow for some of the solvent to evaporate before letting it rotate at 2000 rpm for 25 s in the spincoater.

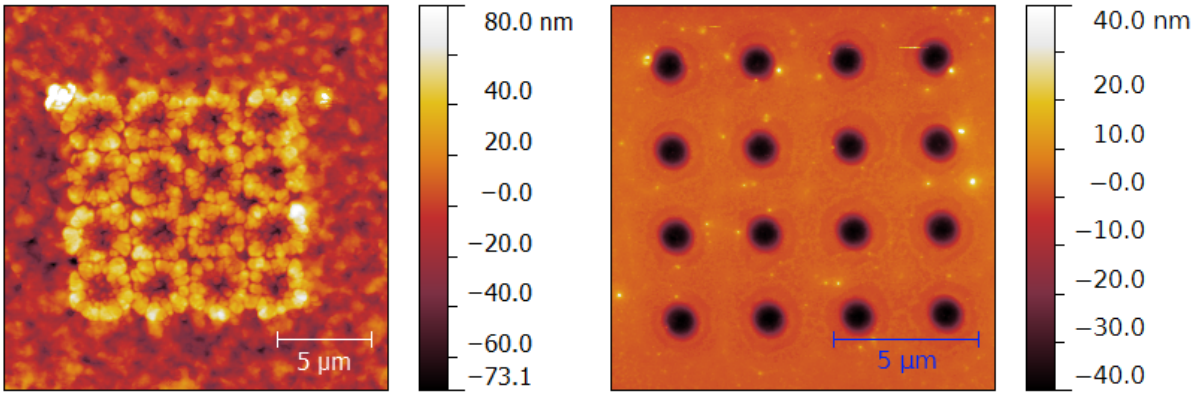

(a) (b)

Figure 15: AFM scans of quantum dot surface structure around a 4x4 array of holes. (a) Due to the high concentration of the quantum dot solution (30 mg / mL), the surface is rough and the quantum dots pile up around the hole edges. (b) For lower concentrations (5 mg / mL), the surface and hole edges of the quantum dot layer become smoother.

Capping Layer Deposition

To protect the quantum dot film from oxidation, a thin capping layer was deposited on the samples after spincoating. The thickness of the capping layer was chosen to be slightly higher than the RMS roughness of the quanutm dot film to ensure adequate coverage without depositing a thick layer that would reduce the minimum separation of the graphene membrane and the quantum dots. Using AFM measurements of the quantum dot film, its RMS roughness was estimated to be 3-5 nm, requiring a capping layer thickness of approximately 7 nm.

To deposit a capping layer, two materials and techniques were tried: alumina

(Al_2O_3) by atomic layer deposition, and silicon dioxide (SiO_2) by evaporation. Low-temperature deposition of alumina by ALD has been reported to protect quantum dots from oxidation by Ihly et al. [48]. However, for the samples made as part of this thesis, it was found that the ALD process damaged the quantum dots, and decreased their fluorescence intensity, deeming the sample unusable for this experiment. The damage to the film is attributed to the hot water vapour and temperature of the sample (80 C) involved in the reaction on the sample surface during ALD, both of which factors are known to damage quantum dots. However, using silicon dioxide evaporation it was possible to coat the sample without damaging it as the temperatures involved in evaporation are quite low at the sample location, and the coating material is in gas phase and does not have to react on the sample surface as is the case in ALD.

Graphene Transfer

After the deposition of the capping layer, graphene was transferred to the samples by a wet transfer process involving liquids such as solvents. Initially, two types of graphene were used: chemical vapour deposited (CVD) graphene and exfoliated graphene flakes. The actual transfer process for each type is described in detail in [53]. CVD synthesis of graphene is a promising candidate for the large-scale production of graphene [54], and allows for the complete coverage of a sample by graphene. This means that many individual devices can be made at one time using suitable samples. For our purposes, this meant that a sample with many holes could potentially yield a large number of suspended graphene devices per sample, as has been demonstrated by van der Zande et al. [23]. However, it was found that when CVD graphene was transferred to samples coated with quantum dots, the graphene coverage was unreliable, as the graphene was strongly wrinkled and torn in many places. Examples of the result of CVD graphene are shown in Fig. 16:

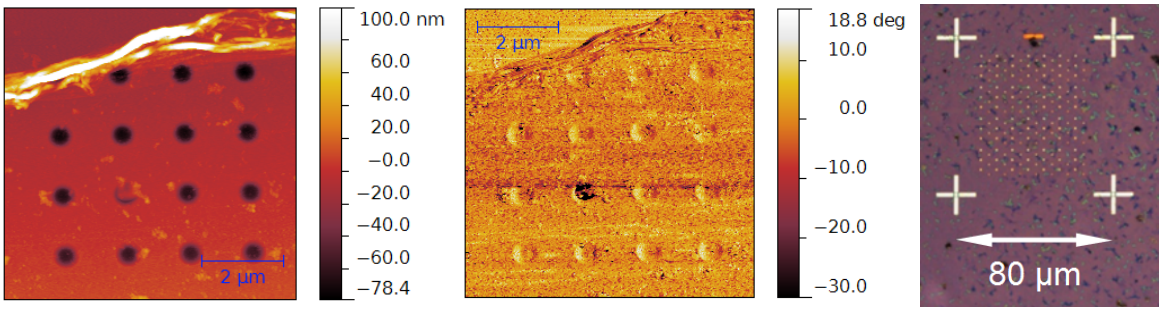

(a) (b) (c)

Figure 16: Transfer of CVD graphene to samples: (a) AFM topology of hole matrix covered by graphene (b) AFM phase showing graphene location (c) Optical microscope image of torn and wrinkled CVD graphene on quantum dots

Exfoliated flakes were the first form of graphene discovered in 2005 by Geim and Novoselov where graphite is repeatedly cleaved using sellotape until only a single layer of graphene remains (exfoliation) [55]. These flakes typically have dimensions on the order of tens of microns, an example of a flake before and after transfer to a sample is shown in . It is clear that the theoretically possible yield per sample is much smaller when a single flake is transferred to it compared to covering it with CVD graphene. However, it was found that the quality of the membranes was higher for samples with graphene flakes transferred to them, for this reason for subsequent samples flakes were used. An example of an exfoliated single-layer flake attached to a multilayer flake and a piece of graphite is shown in Fig. 17a before transfer, and in Fig. 17b after being transferred to a substrate with a hole structure.

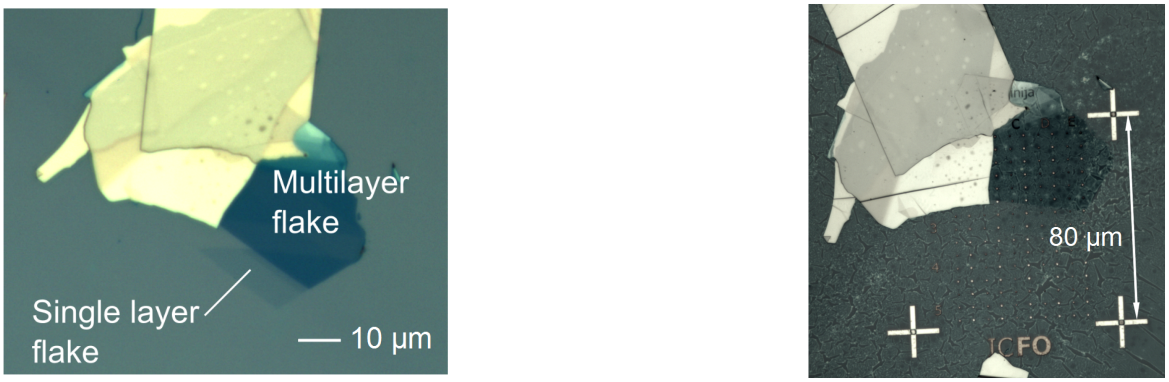

(a) (b)

Figure 17: Graphene flake transfer: (a) Exfoliated flake on substrate before transfer, visible due to interference, causing it to have a light blue hue. The flake protrudes from a bulk of multilayer graphene and graphite. (b) The transferred flake on the sample partially covers some holes on a sample, but is hard to see now due to the underlying substrate now having an additional quantum dot and capping layer.

3.5 Electrical Characterisation of Samples

To electrically contact the graphene membranes and backgate, each sample was mounted into a chip carrier to provide a reliable and robust contact to it in the various characterization setups. As the depth of the chip carrier was significantly larger than the sample substrate thickness, the substrates were stuck to an aluminium square in the chip carrier using silver paste to allow AFM measurements on the sample surface to be made without the risk of breaking the AFM tip on the chip carrier sides. After mounting, the graphene was contacted using a wire bonder.

However, the graphene was not directly wire-bonded, as this would have damaged the sample due to the ultrasonic welding of the gold wire used in the process. Instead, a small length of wire protruding from the wire bonder tip was used as a brush, with which a very thin line of liquid silver paste could be drawn from the graphene edge to a larger contact away from the flake. Here, much care had to be taken not to cover the graphene flake with silver paste in the area of the holes and trenches. The larger contact was made by manually placing a very small drop of thick silver paste on the sample surface with a thin copper wire. Using the wire bonder, a hook-shaped wire was then pushed into the still soft larger contact. When the silver paste became solid, a the wire stuck into it was then wire bonded to a pad of the chip carrier. This technique was used to prevent damage to the sample and to make AFM measurements possible without the graphene area being blocked by wires or large mounds of silver paste. An

example of a contacted graphene flake is shown in 18a.

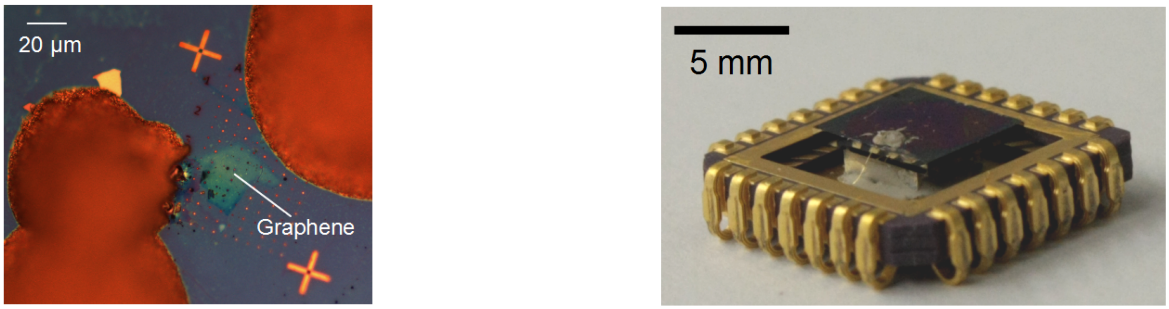

(a) (b)

Figure 18: Silver paste bonding: (a) Doubly contacted graphene flake on hole structure (b) Contacted sample in a chip carrier. The silicon substrate on the aluminium spacer, stuck to the chip carrier base is visible, as well as the silver paste bond and gold wire to contact the flake.

To contact the backgate, a normal wire bond was made connecting the metallic base of the chip carrier with a pad. The doped silicon bottom of the sample being mounted on said aluminium square then ensured good electrical contact. In the wire bonding process, care had to be taken to make robust bonds as the wires traversed relatively large distances across the chip carrier considering their diameter of 25 μm. A mounted and contacted sample is shown in Fig. figure 18b.

An important test of the contacted sample's usability was a leakage test to determine the resistance between the graphene and backgate electrodes, as the applied backgate voltage should not drop across the device. This resistance should ideally be determined only by the insulating silicon dioxide layer on the silicon substrate surface. In this case, a very high resistance is to be expected up to voltages where the electric field across the oxide is strong enough to cause breakdown of the material. The breakdown fieldstrength is given as approximately $10^7\, V\, cm^{-1}$, which means that a layer of roughly 140 nm separating the hole bottom and the silicon substrate would break down upon application of 140 V; this is well above the range of 0-50 V used to deflect the graphene. It is the worst case that only occurs when the graphene flake is deflected to a point where it touches the bottom of the hole, in any other case, the breakdown voltage would be even larger, as the whole thickness of 285 nm of the oxide layer has to be taken into account. However, for real samples, other factors such as the finite conductivity of the quantum dot layer had to be taken into account. This layer could cause leakage currents if the layer went across the edge of the sample and touched the silicon backgate, for example if too much quantum dot solution was used during spincoating.

Leakage tests were performed by sweeping the backgate voltage in a range that should later be applied to the sample, while simultaneously monitoring the current flowing from the graphene on the sample, the principle of the setup used is shown in Fig. 19b: a backgate voltage is applied to the sample, and the current from the graphene flake is amplified and converted to a voltage by a current amplifier . This voltage is then read out as a measure of leakage current. For a typical sample with no leakage, the resistance measured between the backgate and the flake was in the range of 1-200 $G\Omega$, while samples with leakage typically showed resistances of hundreds of $k\Omega$ were measured. These values were measured at voltages of at most 20 V, implying that the current amplifier must have high sensitivity and low noise. The amplifier used (Stanford Research SR570) features an input noise of $5\,fA/\sqrt{Hz}$ and $1\,pA\,/\,V$ maximum gain, thus meeting these requirements.

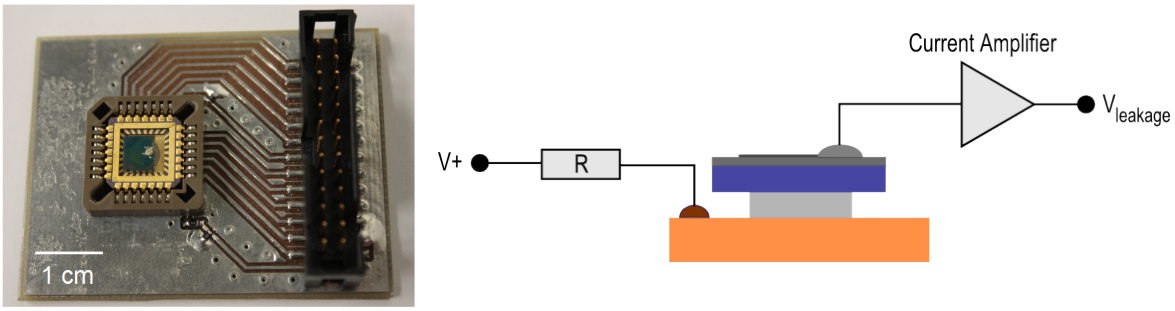

(a) (b)

Figure 19: (a) Chip carrier with mounted sample in sample holder (b) Leakage current test: a backgate voltage ($V+$) is applied to the silicon substrate (blue) via the conductive bottom of the chip carrier (orange) and the aluminium square (grey). The graphene on the silicon oxide layer is contacted via its silver paste bond, and any current flowing is amplified and converted to a voltage $V_{leakage}$, this voltage is then read out. The resistor $R \approx 1\,M\Omega$ limits possible leakage currents that could damage the sample.

3.6 Electrostatic Deflection of Graphene

The deflection of the graphene membranes was performed and measured by scanning the membrane area with the AFM while simultaneously applying a backgate voltage and grounding the graphene flake. To do this, the sample holder with the mounted chip carrier shown in Fig. 19a was placed on the AFM stage and contacted with a shielded ribbon cable attached to a breakout box. This breakout box allowed for all pads to be grounded except for the backgate electrode, so as to avoid any electrostatic charging of parts of the sample or chip carrier that could influence the membrane behaviour.

Furthermore, the sample holder was designed so that all striplines from the ribbon cable connector to the chip carrier had grounding leads surrounding them for shielding, and the shielded ribbon cable also suppressed any influence from stray electric fields.

To measure deflection, scans of the membrane were performed at 0 V, then at a series of voltages, and finally at 0 V again. This last scan is essential to show that the membrane moves back to its initial position after having been deflected, to make the measurement reproduceable. When applying higher voltages to the membrane, it is important that the voltage is increased slowly to avoid spikes that can damage the membrane and cause leakage of the whole sample in the worst case. For the devices shown here, a rate of 1 V / s was chosen as a maximum rate of voltage change; this also had to be kept in mind for scripts involving automated voltage changes.

4 Results and Discussion

4.1 Sample Structure

Hole Structures

Before making samples with quantum dots and a capping layer, the characteristics of suspended graphene were studied. To do this, samples with holes of different depths are directly covered with graphene. An example is shown in Fig. 20, where a matrix of 16 holes with 500 nm diameter and 135 nm depth is covered by CVD graphene to study the membrane properties. The optical microscope image in Fig. 20a shows the hole matrix at the centre of a large area of graphene, visible due to its blue hue. From the optical image, it seems that the holes are completely covered by graphene.

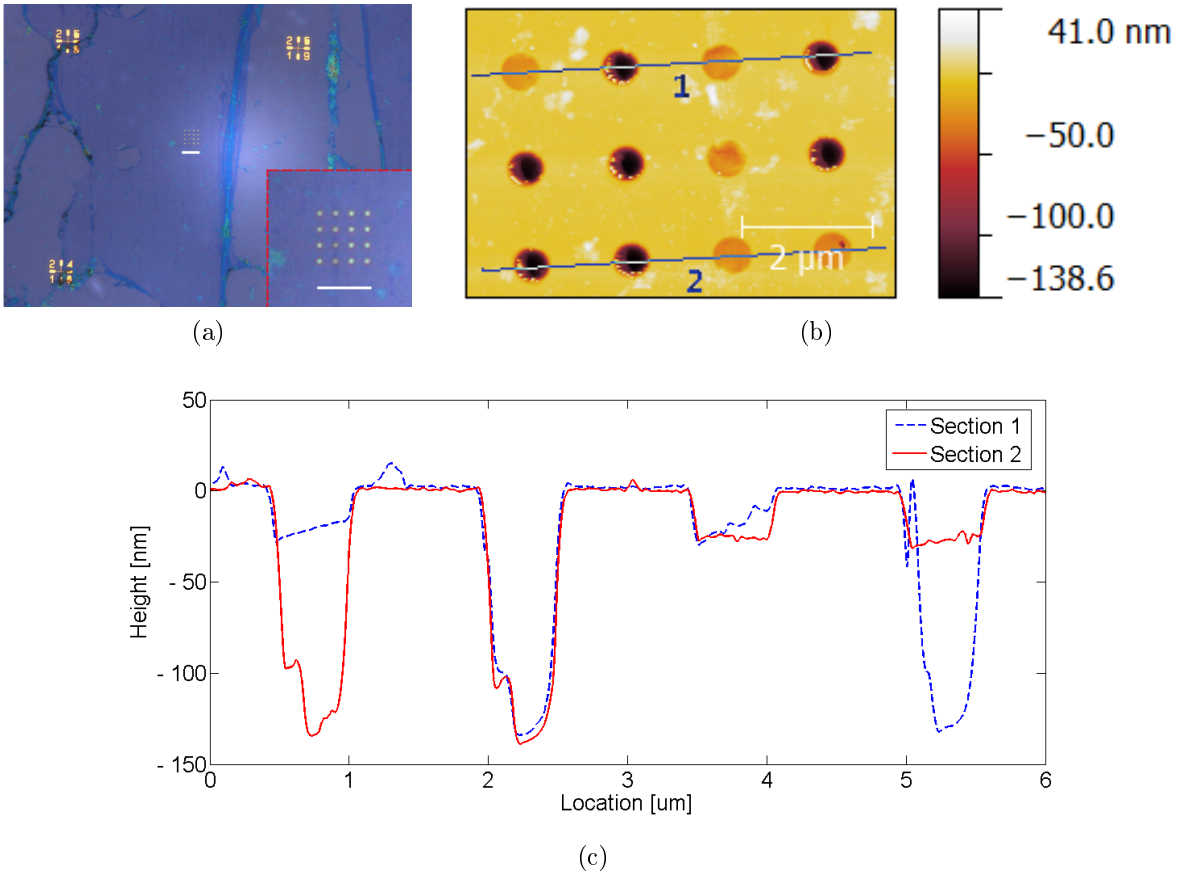

(a) (b)

(c)

Figure 20: Circular graphene membranes suspended on 500 nm diameter holes of 135 nm depth : (a) Optical image with inset detail of hole structure (white scale bar 8 μm), (b) AFM topology. (c) Line sections through AFM scan. Suspended and collapsed graphene membranes are clearly visible for both hole diameters.

In Fig. 20b, an AFM scan over three of the four rows of holes is shown. Here, it becomes clear that only approximately half of the holes are covered in graphene to form suspended membranes, while the graphene seems to have collapsed into the others. The sample surface has some impurities that also partially cover the membranes. Two sections through the topology in Fig. 20b are shown in 20c. The sections indicate that the hole depth and structure are similar across the area of the hole matrix, and also that the membrane shape is very similar for different holes. In this case, the profile of the hole bottom is that of the graphene which has collapsed into it. Surprisingly, the shape of the collapsed graphene is very similar for all the holes with broken membranes. This is also visible in the topology scan; the deep (dark coloured) holes all have small, high features at one side, this is the collapsed graphene forming a wrinkle at the hole bottom. The fact that this wrinkle seems to be at the same side of each hole indicates that the breaking of the membranes may be due to a tension in the graphene in one direction, which may happen during the transfer.

The sides of the holes appear to be slanted, even though the FIB makes surface sides perpendicular to the substrate surface. A further reason for the slanted appearance of the side walls is that any image of a topology using an AFM is the convolution of the tip profile with that topology. This means that for structures with very steep, perpendicular faces, these faces will appear to have at least the slant of the AFM tip, as this is not a perfect point probe, but has a gradient from its base to the tip as shown in Fig. 9a. The angle between the apex and base of the tips used are on the order of 15° - 25° depending on the face considered [51], which corresponds to the maximum sidewall steepness measured. Ideally, this angle should be 0° for an infinitesimaly narrow tip.

There are a total of four suspended membranes visible in the sections in Fig. 20c, with similar structures. Each membrane features a sag of roughly 30 nm. This is attributed to various factors: For one, the graphene is stuck to the side walls of the holes to a certain extent before becoming a membrane by van der Waals forces caused by interatomic attraction between the graphene and the silicon dioxide. This means that the area of graphene on the hole is larger than the area of the hole face itself, allowing it to stick to the sides instead of forming a taut membrane. The cause of this surplus area of graphene is thought to be the wrinkling of graphene on surfaces, as discussed in previous sections. This wrinkling is also visible in the shape of the membranes themselves; only two of the membranes actually have a flat base that is parallel to the surface and therefore also to the hole bottom. It is noteworthy that the graphene on the substrate surface seems relatively flat, this is again due to the van der Waals forces that attract it to surfaces, but that are absent under the suspended membranes.

Data such as that shown above was collected for different hole diameters, and the membranes were characterized as is done in the above example, resulting in a collection of average membrane sags for different hole diameters. The hole diameters used were 250 nm, 500 nm, 750 nm, 1 μm, 1.5 μm and 2 μm. However, of these not all hole matrices were covered due to tearing of the CVD graphene sheet, causing the data for 1.5 μm diameters to be missing. The data collected is shown in Fig. 21, together with a linear fit which is used to choose the diameters of the holes for samples with quantum dots and capping layers.

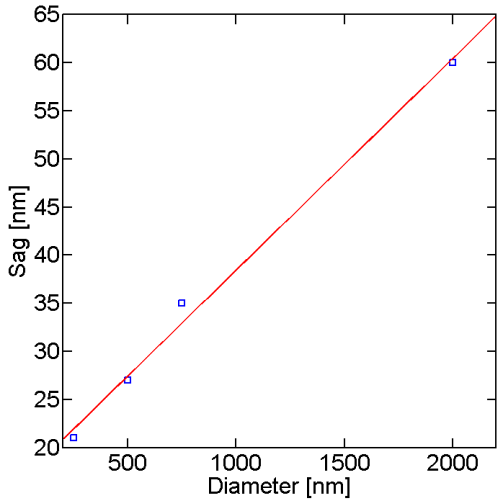

Figure 21: Measured (blue squares) and fitted (red line) sag of suspended graphene membranes for various hole depths.

Based on the observation that membranes of CVD graphene are often broken, samples are made using exfoliated graphene flakes. The substrate area covered by a flake is limited by its small size in the range of tens of micrometers. This means that samples are designed such that all hole diameters can be covered by a single flake; the structure used is shown in Fig. 22. Based on the analytical electrostatic deflection model, holes with diameters of 750 nm and 1 μm are made, as these are predicted to deflect by more than 20 nm for backgate voltages of up to 50 V without being too sensitive to small changes in voltage (see Fig. 6). The topology of one design used is shown in Fig. 22a, together with its depth profile (Fig. 22b). The hole depths measured are 130 nm, 100 nm and 80 nm for the 750 nm diameter holes 140 nm, 110 nm and 100 nm for the 1 μm diameter holes.

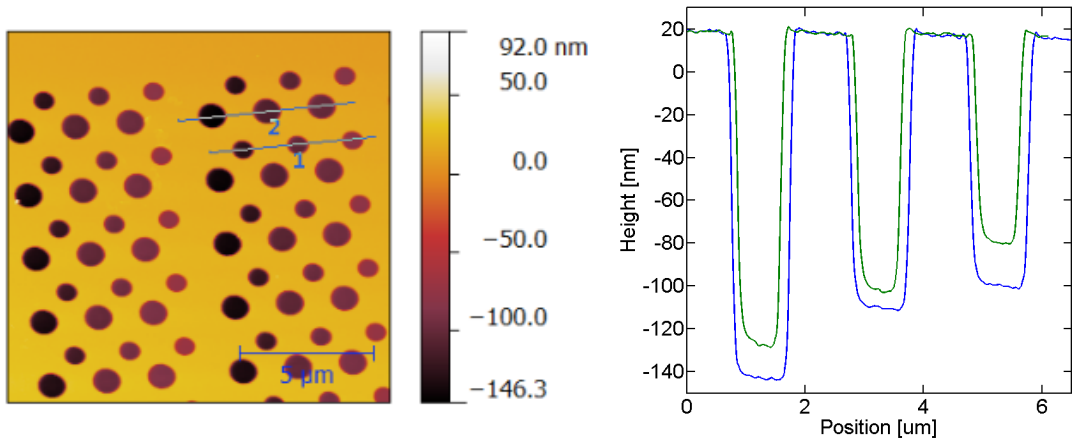

(a) (b)

Figure 22: Sample hole structure and depths: (a) AFM topology of 750 nm and 1 μm diameter holes with line section locations (b) Line sections of 750 nm (green) and 1 μm (blue) holes.

For deflection measurement, the above design is slightly modified by increasing the separation between the individual holes to 5 μm. This is done to give the graphene more area to adhere to the substrate between holes to try and make the membranes tauter. The FIB flux doses used to make the holes are the same as those used for the above structure, resulting in depths of 145 nm, 120 nm and 96 nm for the 750 nm diameter holes, and 160 nm, 130 nm and 115 nm for the 1 μm diameter holes. A scanning electron microscope (SEM) of this design is shown in Fig. 23. For these samples, markers and a coordinate system are also milled into the substrate surface to allow for easier location of the patterned area and individual holes inside it using optical instruments.

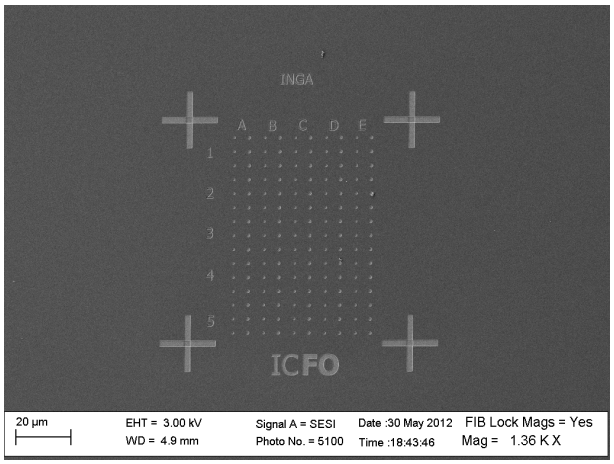

Figure 23: SEM image of sample design: each row of holes is a repeated pattern of three depths (see text).

In Fig. 24a, we see an AFM scan of a sample similar to the ones described above but coated with PbS quantum dots following the procedure described in Section 3.4. The depths shown now include contributions from both the additional layers of quantum dots in the holes and on the surface. From the line sections one sees that the coated holes closely follow the structure of the uncoated holes, with a difference in depth of 15-20 nm between each hole of a given diameter. The roughness of the quantum dot surface can also be extracted from this data, yielding an RMS value of 2.9 nm on the substrate surface.

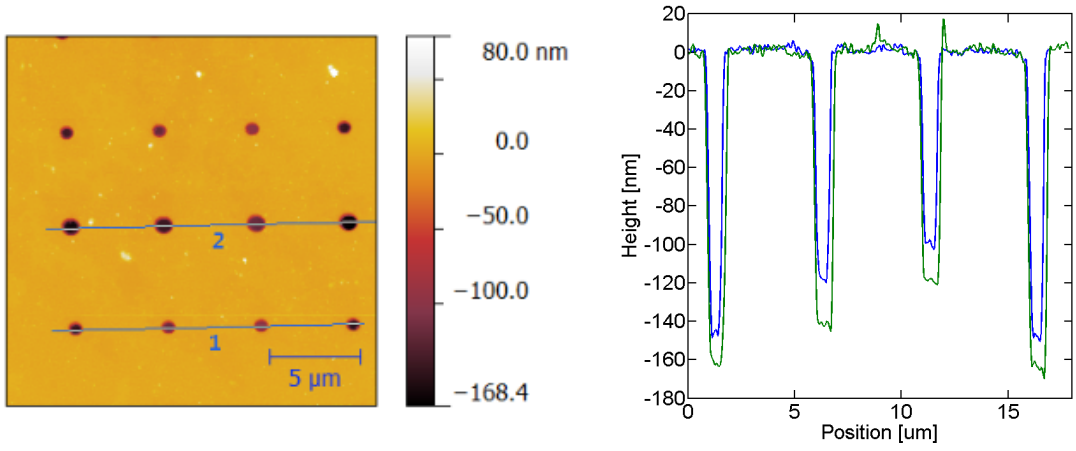

(a) (b)

Figure 24: AFM scan of a sample coated with PbS quantum dots: (a) Topology (b) Line sections of 750 nm (blue) and 1 μm (green) holes. The original hole structure and depths remain clearly visible after the coating.

The quantum dot layer thickness in the holes is found by scratching a coated sample with a syringe tip and measuring the height of the quantum dot layer on the sample surface. Knowing the depth of each hole before and after the coating process, one can then deduce the height of the coating in the holes. The height measured using the AFM is found to be 17-20 nm. As the measured hole depths of the coated and uncoated sample are identical to within a few nanometers, it is assumed that the height in the holes is the same.

Trench Structures

Trench structures with similar depths to the previously described hole structures are also fabricated. They consisted of concentric rings with alternating widths of 750 nm and 1 μm, forming a "bullseye" structure. These structures are made to study whether the transfer of graphene to holes caused the liquids involved to be trapped in the hole. If this were the case, the quantum dots in the holes would be damaged by contact with the liquid and the deflection of graphene would be hindered by it. In a trench, it is assumed that any liquid under the graphene would not be trapped there, and could evaporate. Furthermore, the trench structures offer the possibility of studying the deflection of doubly clamped membranes, which require less force to achieve a given deflection than a fully clamped, circular membrane. The clamping of the membrane in this case is due to its sides being stuck to the substrate surface by van der Waals forces.

The trench structures fabricated are shown below as an SEM image Fig. 25. The advantage of this concentric ring structure over straight trenches is that for a given random position of a graphene flake transferred to it, the probability of the flake covering many trench widths and depths is higher, while still allowing the trenches to be spaced reasonably far apart by 5 μm.

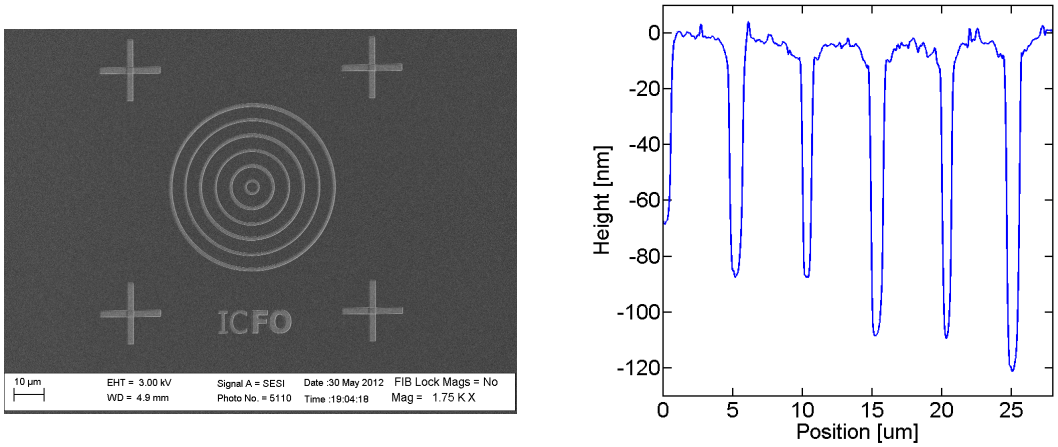

(a) (b)

Figure 25: Bullseye sample: (a) SEM image of trench structure made of concentric rings of alternating 750 nm and 1 μm widths. The rings are radially equispaced by 5 μm (b) AFM line section of coated sample, showing the quantum dot surface to follow the trench structure well.

Capping of Quantum Dots

To study the protection of quantum dot films capped by a thin layer of SiO_2, two unstructured samples are spun-cast with quantum dots in the way described previously in Section 3.4, and then one of them is coated with a 7 nm thick layer of the oxide deposited by evaporation. First, the intensity of photoluminescence is compared for the two samples. This is done using the scanning setup previously described, with the addition of placing the sample in a stream of dry nitrogen to reduce the effects of oxidation and water absorption from the air. In Fig. 26, we see the PL scans of both samples. In each scan, a small square scan was performed, followed by a larger scan that included the previous one to compare the photobleaching behaviour of the two samples.

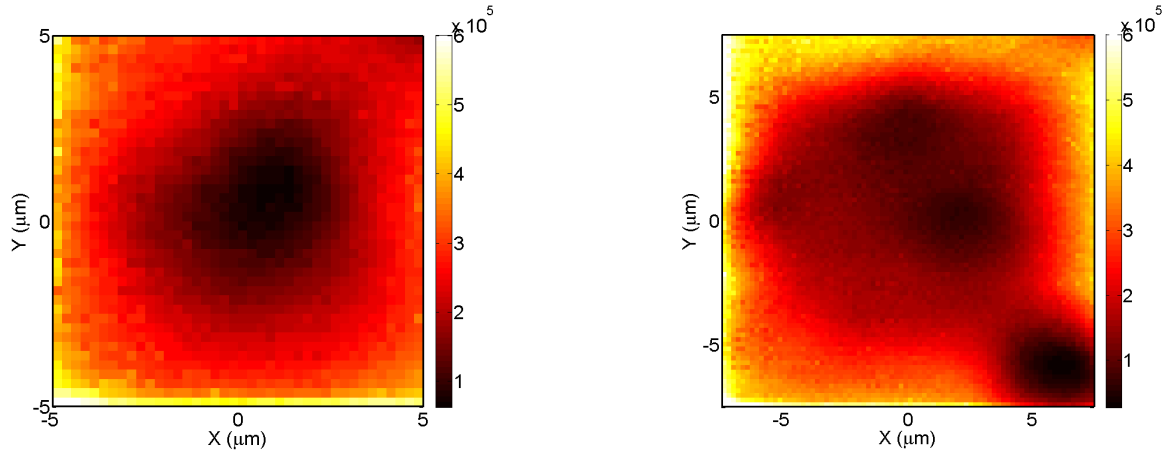

(a) (b)

Figure 26: Quantum dot PL intensity: (a) Uncapped layer (b) Capped layer. The images show the emission after a first scan is performed in the central area, followed by a second scan of a larger area to check the bleaching caused by the first scan. The area chosen for the first scan in (a) is a square of 3μm sidelength centered on the origin, in (b) the first scan area is a larger square of sidelength 10 μm also centered on the origin. The capped sample has a higher emission in the doubly scanned area of approximately $1.8-2\,10^5$ cps compared to the uncapped sample with approximately $0.8-1.5\,10^5$ cps.

The covered quantum dot layer shown in Fig. 26b has a higher PL intensity than the uncapped one in Fig. 26a, especially in the bleached (darker) central area. This is important so that multiple measurements can be performed on a given sample without premature bleaching. The time between spincoating, capping and PL scanning is approximately three hours, during which the uncoated sample is kept in a desiccator to minimize water absorption from the air. The comparison of the bleaching behaviour leads to the conclusion that the capping layer does indeed reduce the damage to the quantum dot layer by atmospheric oxygen and humidity, for which further samples are capped.

Besides the protection from atmospheric influences, the capping layer also protects the quantum dot film from the solvents and other liquids used during the wet transfer process of graphene. This was investigated again by making a capped and uncapped sample, and processing them in a simulated transfer, where both were suscepted to the chemicals involved in flake transfer, but no flake was actually transferred. Any change in lifetime due to this process is important as this is what is later measured to observe resonant energy transfer. In Fig. 27 below, lifetime histograms for capped and uncapped quantum dot films before and after the simulated transfer are shown. The histograms are normalized to their maximum so that the effect of higher PL intensity

is suppressed here.

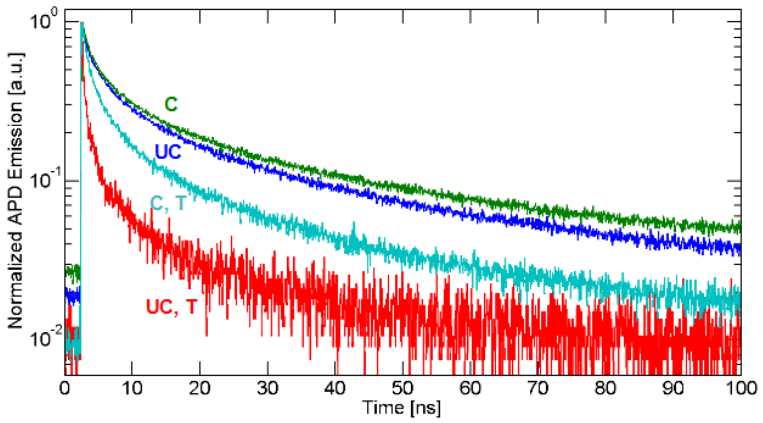

Figure 27: Lifetime histograms of capped (C) and uncapped (UC) quantum dot layers on a substrate before and after simulated transfer (T). The capping process increases the intial decay of the emission after the excitation peak, while the transfer process affects the decay on the time scale of approximately 10 ns after the maximum.

Comparing the histograms shown above, one can deduce the effect of the transfer and capping process on the lifetimes of the emitters. The transfer process affects the decay in the first 0-5 ns after the maximum, while the capping layer increases decay on the time scale of 5-20 ns after the peak, this leading to the slower total decay of the capped emitter. In total, the capping and transfer process seem to have the largest effect on the fast decay of the emitter, but this change carries through to yield longer total lifetimes for the capped emitters.

It was observed that the structure of samples with capped quantum dots was quite different to the structure of the capped layer on the reference sample. The roughness of the coated quantum dot layer went from 2.9 nm RMS to 5.9 nm RMS for the capped layer on the sample surface. More importantly, for some samples, the roughness inside the holes or trenches strongly increased after coating. The trench structure shown in Fig. 28adisplays this, a comparison of the uncapped and capped trenches is also shown. Here, it is clear that the capping makes the trenches much rougher, causing them to lose their smooth shape almost entirely. The section shown is a representative one as the shape of the trench varies strongly for different positions of the section along it. To quantify this, the roughness over the area of the innermost ring was taken and found to be approximately 20 nm RMS. Similar values are to be expected for the outer trenches, as this roughness should not depend on the location of the trench. in the structure.

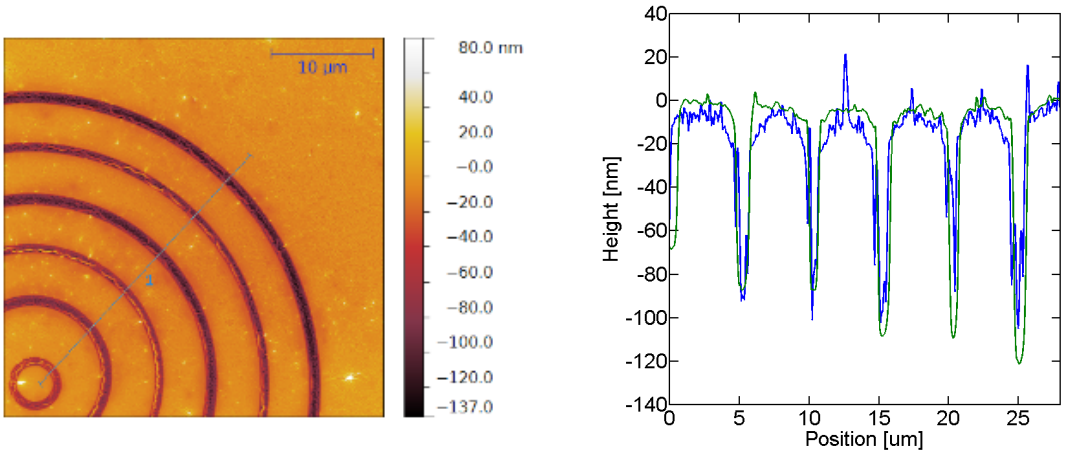

(a) (b)

Figure 28: Capping of trench structures: (a) AFM topology (b) Linescan comparison before (green) and after (blue) deposition of capping layer on sample. The roughness of the trench profiles increases strongly after the capping process.

For samples with holes, a different change of surface was observed: upon deposition of the capping layer, their surface was entirely covered with fissures. These fissures formed a network that split the sample surface into islands where it was smooth, separated by cracks; an example is shown in Fig. 29b. These fissures appeared shortly after the oxide layer deposition - we attribute them to the effect of temperature and humidity. The surface structure is however improved by using a slower deposition rate (see Fig. 29b), yielding a surface roughness of 5.8 nm RMS as before.

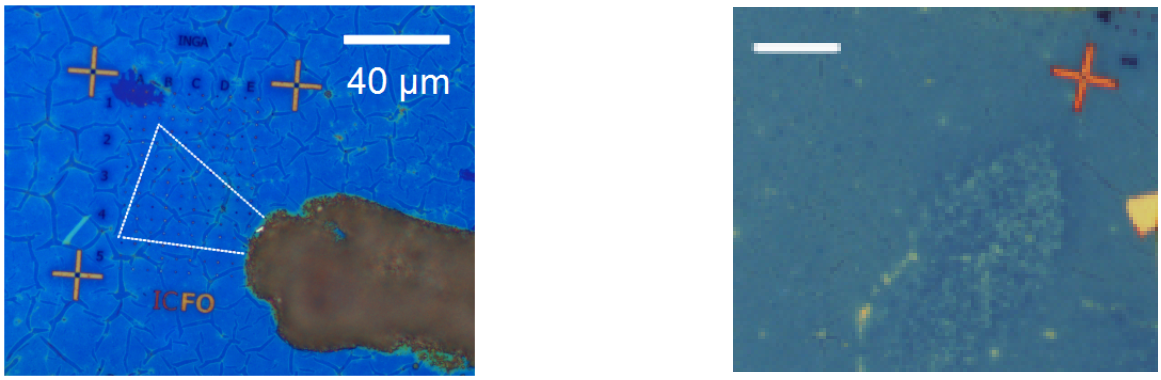

(a) (b)

Figure 29: Optical microscope image of: (a) a contacted sample with holes, with large cracks forming islands with a smooth surface. The location of the graphene flake is indicated by the white dashed lines.(b) a detail of a capped hole structure coated with a slower deposition rate. Scale bar: 10 μm

Despite slower deposition rates, the structure of the hole bottoms was still uneven as is shown in Fig. 30 where it appears that only the deepest holes retain their profile after capping. Again, the capping seems to cause the hole depth to change locally by much more than the thickness of the deposited layer, in some cases such as the hole shown at position 17 μm in Fig. 30 , where the capping reduces the hole depth to about one third of its original value. This change is much larger than the thickness of the capping layer itself, suggesting that other effects apart from the roughness of the deposited material cause this change of profile. Most of the deflection measurements performed in the next section are therefore performed on the deeper holes, as the membranes do not touch the hole bottom there.

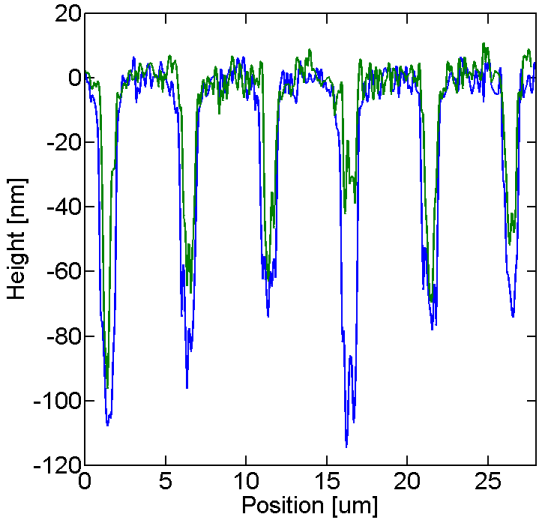

Figure 30: Line sections of 750 nm (green) and 1 μm (blue) holes after capping with a 7 nm silicon dioxide layer. The depth profile of the original sample structure is still followed, but the hole bottoms are much rougher, exceeding the deposited layer thickness by far.

Suspended Graphene on Quantum Dots and Capping Layer

As has been shown, the surface of samples coated with capped quantum dot layers is quite different to the uncoated, structured substrates. This also affects suspended graphene membranes, especially if the sag of the membranes is large enough for them to touch spikes on the hole bottom such as those shown in Fig. 30. If this happens, the membrane partially sticks to the peaks in the hole due to van der Waals forces, thus completely changing its structure. Even if the sag of the suspended membrane is low enough for it not to touch the hole bottom initially, deflection may cause it to do so when a certain voltage is applied. This prevents the membrane from returning to

its inital position without an applied electrostatic force and also from approaching the quantum dot layer close enough to be able to see any change in decay rate due to to resonant energy transfer.

In Fig. 31, an array of holes covered in capped quantum dots is shown, covered by a graphene flake, together with two line sections that show membranes on 750 nm and 1 μm holes. The AFM topology shows clearly the location of the graphene flake in the right half of the image, lying on a slightly fissured sample surface. The flake itself is also wrinkled at various locations. The line sections reveal the structure of the membranes and holes, as previously discussed. It is noteworthy that the structures of the holes are very similar for both diameters, apart from their depths. This is caused by the quantum dot and capping layer, as well as the cracks in the surface that are still present. For this reason, the two pairs of membranes on the graphene look very similar, and also have the same sag of approximately 60-80 nm. This is larger than expected for the nominal diameters (see Fig. 21), but can also be attributed to the changed hole shape.

As discussed previously, the sag of membranes is partially caused by the graphene sticking to the side walls of holes by van der Waals forces. In the case of an uncoated sample, the hole walls are much steeper compared to the sample shown. Therefore, the graphene on coated holes can stick to the side walls further into the hole, causing a larger sag. However, this also leaves less graphene to wrinkle at the bottom of the hole, producing a smoother but more parabolic shape compared to membranes on holes with well-defined, perpendicular sides.

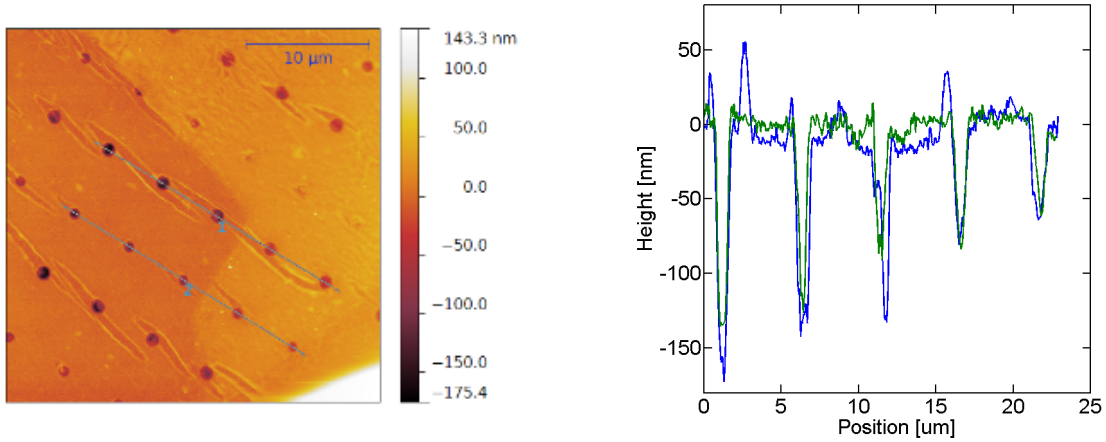

(a) (b)

Figure 31: Graphene flake on capped quantum dot layer: (a) Topology (b) Line sections through covered and uncovered holes of 750 nm (green) and 1 μm (blue). Covered hole can be identified by the periodicity in the hole depth: every third hole should have the same depth; if this is not the case, the hole is covered by graphene. A further indicator is that covered holes of the same diameter should also have the same depth.

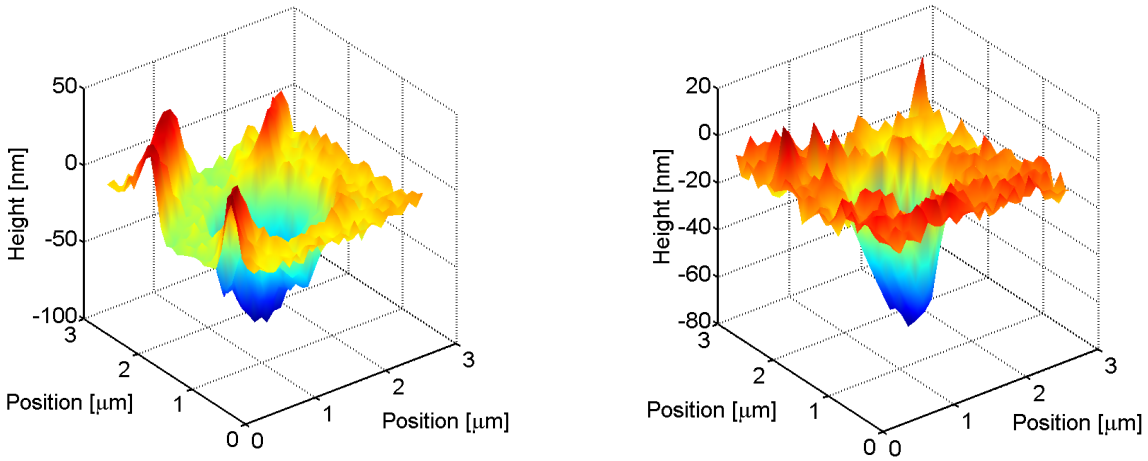

(a) (b)

Figure 32: 3D Plots of AFM scans of suspended graphene membranes on capped quantum dot layer: (a) 1 μm diameter, (b) 750 nm diameter

Fig. 32 shows two 3D plots of graphene membranes of 1 μm (Fig.32a) and 750 nm (Fig.32b) together with the surrounding surface structure, taken from AFM data. It is clear here that the surface surrounding the hole is quite uneven, causing the membranes to have a shape different to the ideal parabolic one for a thin film on a flat-edged hole.

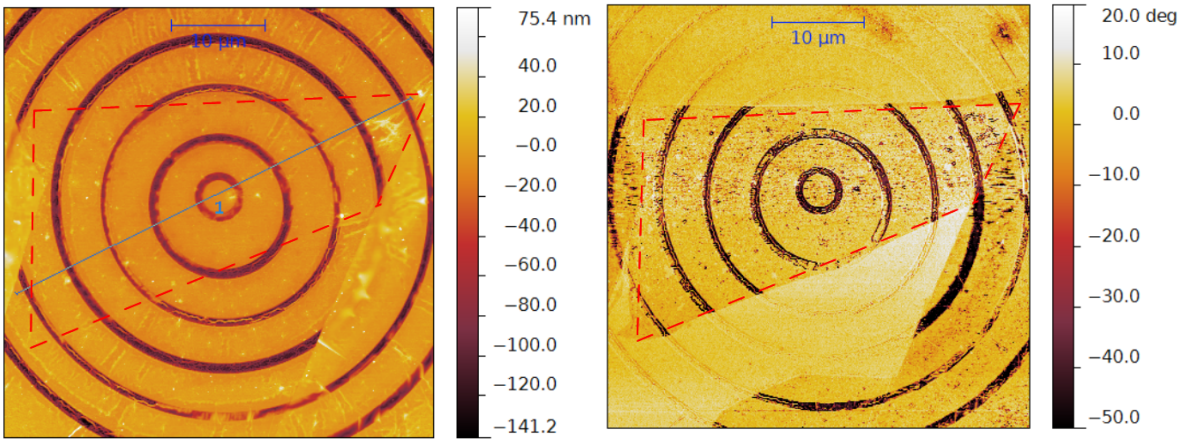

(a) (b)

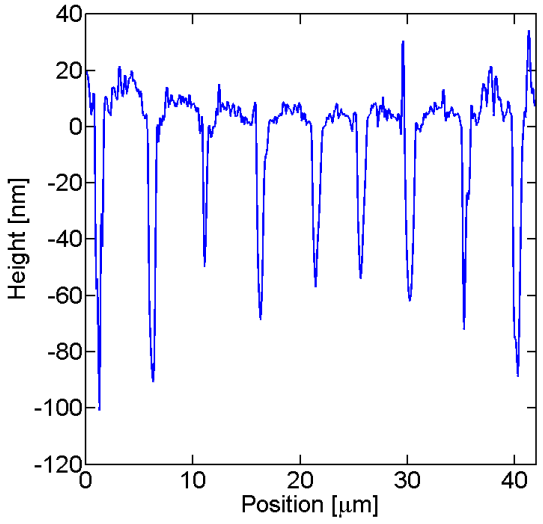

(c)

Figure 33: AFM scans of graphene flake on a Bullseye trench structure: (a) topology with line section location (blue line), (b) phase, (c) line section. In the line section, the hole depth increases from with increasing position values up to the center at 23 μm, where the depths increase again due to the symmetry of the Bullseye structure. Covered trenches are visible by their decreased depth, such as that at position 12 μm, with a sag of approximately 60 nm.

The structure of a sample with trenches is shown in Fig. 33. While the flake is not clearly visible in the topology scan Fig. 33a, the phase image Fig. 33b shows it clearly as those areas where the phase is non-uniform, for clarity this area is also enclosed by a dashed red line in both images. The section in Fig. 33c shows the profile of the first, second and third rings with trench widths of 750 nm, 1 μm and 750 nm, respectively. The sag of membranes on the 750 nm wide trenches can be seen for the

trench at position 12 μm; it is in the range of 60 nm. This is close to the depth of the 750 nm diameter central ring, and means that the graphene in the innermost ring almost touches the hole bottom at the location of the line section. The same is true for the trenches at position 17 μm and 31 μm that are part of the 1 μm wide second ring. The depth of the graphene there is in the range of 70 nm, compared to their nominal 80 nm depth after capping (see Fig. 28b).

4.2 Protection of Quantum Dot Layer by Graphene

During initial PL scans of the fabricated samples, it was found that the emission from the quantum dots directly under the graphene flake was significantly stronger than that of the surrounding area. For the results shown here, we concentrate on the central area of the covered structure where the flake is single-layer, inside the area marked approximately by the dashed red lines. Below, two PL scans of the same area before and after numerous scans of that area are shown in Fig. 34, taken using a laser power of 10 μW and a repetition rate of 5 MHz.

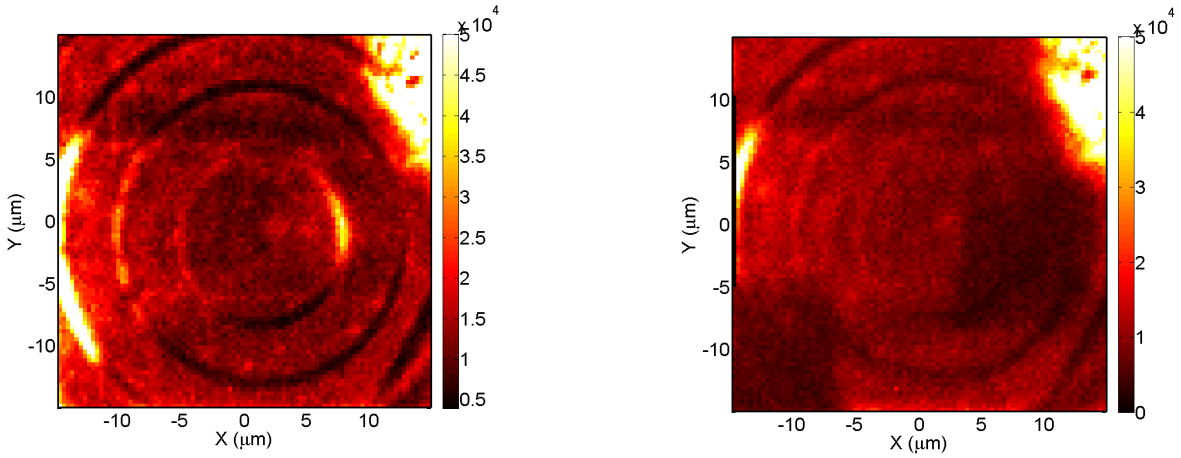

Figure 34: Comparison of PL image of graphene flake covering Bullseye trench structure: (a) initial scan performed after fabrication (b) scan of same area after many PL scans. An overall reduction in emission intensity is visible after scanning, and the contrast between the covered and uncovered areas is reduced. However, the effect of the graphene protecting the quantum dots in the trenches is still visible, as the emission there is still higher than in the uncovered area. Two square areas of very low emission are visible in the the second scan, these have been scanned over a long period of time during more detailed studies of the emission, thus a strong bleaching effect has set in.

From the PL image of the flake before being scanned multiple times (Fig. 34a), one

can see that the photoluminescence in the area covered by the graphene is stronger than in the uncovered area; this is true for the substrate surface as well as in the trenches. First, we concentrate on the area covered by the flake: here, the difference in emission strength in and outside the trenches is clear; the emission from the trenches is much higher. This is a first indicator of the effect of the distance of the graphene on the fluorescence properties of the quantum dots, as the distance from the graphene is larger in the trenches than outside, where fluorescence is quenched by graphene. As discussed in Section 4.1, the membranes of the inner two circles touch the capping layer - for this reason they do not appear bright in the above PL images in many places. The distance between the graphene and the quantum dots is then only given by the thickness of the capping layer, thus the fluorescence is quenched to the same extent as on the substrate surface.

The fact that the emission under the graphene flake is higher than from the surroundings even where the quantum dots are directly under the flake suggests that graphene protects them from some bleaching mechanism - this is also verified by lifetime measurements (see Fig. 4.4). It is surprising, considering that the quantum dots are covered by a capping layer that should protect them from damage by solvents or oxidation. Graphene fluorescence cannot explain this increased emission as it requires significantly shorter excitation pulses of the order of tens of femtoseconds [56]. This leaves photobleaching as a possible mechanism that can occur in the absence of other reagents that damage the quantum dots, however it is unclear how the graphene protects the emitters from this.

The next PL image shows the same area after having been scanned many times, especially in two square areas of 7 μm side length, centred on the points (-10,-10) and (8,-2). Accordingly, some bleaching has caused the overall emission to decrease, especially in the square areas. However, the emission under the graphene flake is still slightly higher than that of the surroundings, and importantly the emission from the trenches is still relatively high, though some contrast is lost. In terms of the structure of the membrane on the trenches, this also means that the edge of the membranes must touch the bottom of the trench to isolate the quantum dots underneath the graphene from the surroundings - if this were not the case, any solvents or liquids could enter under the membrane, causing the quantum dots to behave just as their counterparts in the uncovered area. This can be verified with the AFM scan in Fig. 33a where the flake edge is seen to be touching the trench bottom.

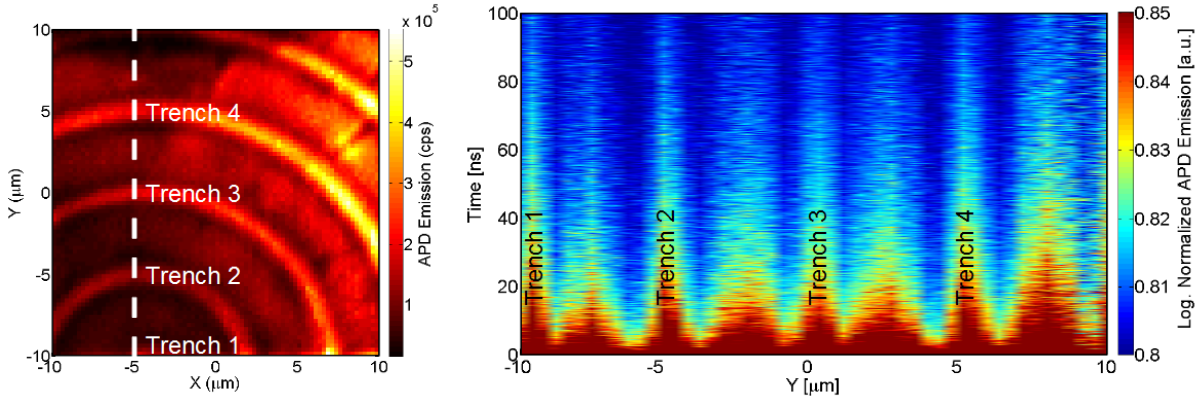

(a) (b)

Figure 35: Lifetime linescan: (a) PL scan with line scan location (dashed line). (b) Lifetime histograms along the line scan. The locations of the corresponding trenches in the PL and histograms are marked "Trenches 1-4".

The effect of graphene on the quantum dot emission properties is also detectable by measuring lifetimes. For example, Fig. 35b shows normalized lifetime histograms plotted logarithmically along a line scan through a number of trenches, and the location of the scan is shown in the PL scan in Fig. 35a. The decay of the lifetime is slower at the locations of the trenches, again due to the larger separation of the graphene and the membrane at those points, leading to less quenching than on the substrate surface. An increase in lifetime is also visible in the central areas between two trenches which follows the emission intensity along the line scan. This may be due to a reduced concentration of quantum dots around the trench edges, or possible also graphene wrinkling there, leading to less quenching.

4.3 Electrostatic Deflection Control

To electrostatically control and detect the deflection of graphene membranes by a back-gate voltage applied to the sample, the procedure described in Section 3.6 was followed. For deflection measurements performed using the AFM, hole structures were used as they provide a more well-defined membrane shape compared to the trench structures, which are quite irregular due to the underlying trench structure. The AFM scans acquired in this way for each voltage were first analysed using line sections through membranes which should yield the shape and vertical displacement of the deflected membrane. However, due to the roughness of the membranes, the shape of the line sections was highly variable depending on its location. The error made by using one

representative line trace to describe the shape of a whole membrane is on the order of or even larger than the deflection to be expected, therefore this method cannot be used to reliably measure the membrane deflection.

Instead, a statistical approach was used, where histograms of the height distributions of the membrane area and a reference area were compared for each value of the applied voltage. This was done by first leveling the AFM data around the hole area, and then selecting a square area inside the membrane and a square reference area close to the hole but away from the crater-like structure surrounding it. The data inside these areas was split into 10-20 bins of depth ranges, thus yielding a histogram of the depth distribution. The number of bins was chosen such that the histogram was accurately resembled by a Gaussian bell shape, however it was found that this did not have much influence on the value of the mean of the fit. The reference area was chosen to include a small particle on a flat surface so that the corresponding histogram would be narrow. An example of the membrane and reference areas is shown in 36.

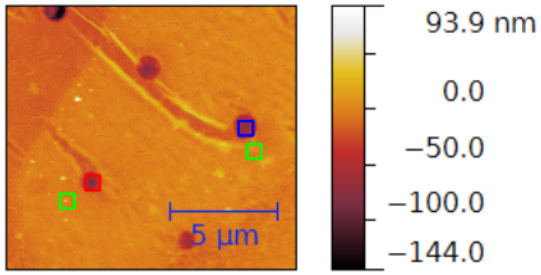

Figure 36: AFM map with areas used for histogram data: 750 nm (red square) and 1 μm (blue square) membrane and respective reference areas (green squares)

The membranes shown were deflected by applying backgate voltages of 0, 10, 15 and 20 V to the backgate of the sample while grounding the flake. After reaching 20 V, a final scan was performed at 0 V again to verify that the membrane returns to its original undeflected height at 0 V. The membrane and reference histograms acquired in this way for the 750 nm diameter membrane are shown in Fig. 37, together with their Gaussian fits. The separation of the two histograms with increasing values of applied backgate voltage can clearly be seen as well as the movement to the membrane's original distribution when sweeping back to 0 V.

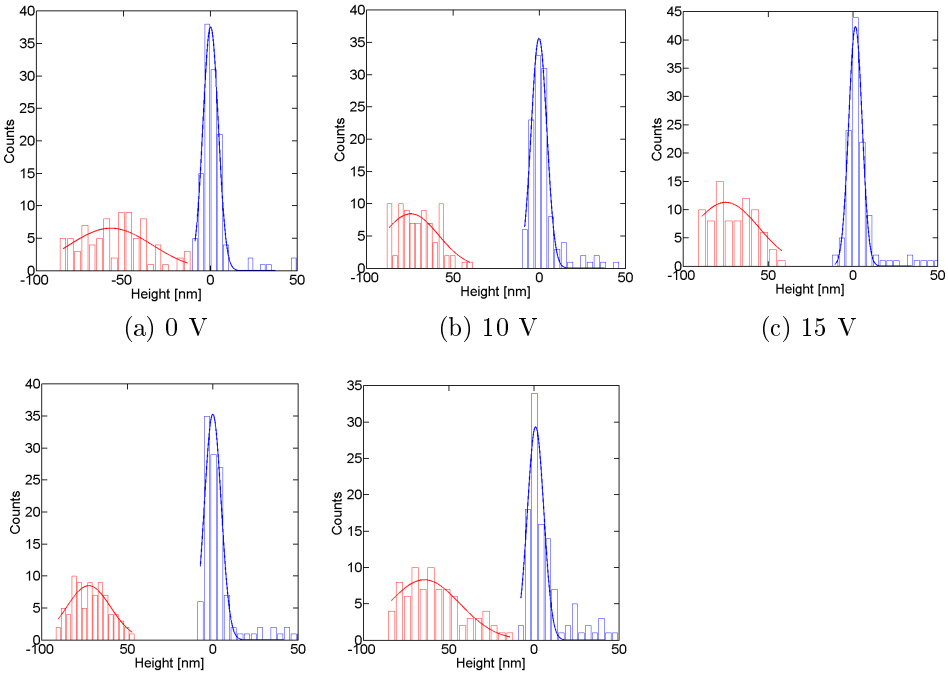

(a) 0 V (b) 10 V (c) 15 V

(d) 20 V (e) 0 V Backsweep

Figure 37: Histograms and Gaussian fits of the height distribution of a 750 nm diameter membrane (red) and a reference area on the sample surface (blue) for different applied backgate voltages

To quantify the deflection of the membrane, both the membrane and reference histograms were fitted to a Gaussian distribution. The difference between the means of the two Gaussian fits then serves as a quantitative estimate of the mean height difference between the membrane area and the reference area. This difference is plotted below for a 750 nm and 1 μm diameter membrane as shown in Fig. 36; here, the data for the 1 μm membrane was obtained in the same way for the 750 nm membrane. In the same plot, the analytical model for the value of the maximum deflection of the membrane is plotted. For this, measured values of parameters such as hole depth, quantum dot and capping film thickness as well as membrane sag were used.

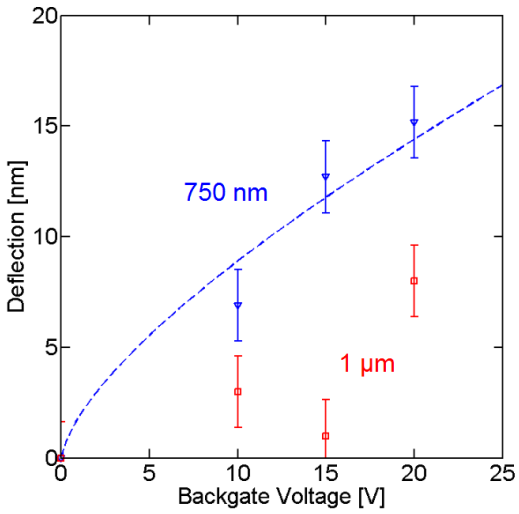

Figure 38: Measured (points) and simulated (dashed line) deflection of 750 nm (blue) and 1 μm (red) diameter membranes against applied backgate voltage. The 750 nm diameter membrane follows the simulated values well, while the data of the 1 μm diameter membrane suggests that it is broken.

Comparing the plots, it is clear that the 750 nm membrane behaves as expected, increasing monotonically with backgate voltage, while the 1 μm membrane behaves more erratically. This may be caused by the structure of the membranes - while the smaller one has a smooth surface and base, the larger diameter one is very wrinkled (see Fig. 32). During deflection, it is possible that some of the deflective force causes a very wrinkled membrane to change its shape, without any net deflection of the whole membrane surface. The data shown for the 750 nm diameter membrane fits the model plot quite well. However, it is not expected to follow it exactly, as the model describes the dependence of the maximum of displacement of a parabolic membrane with backgate voltage. The histogram mean depends on the movement of the whole, wrinkled membrane with contributions from parts of the membrane that are far from the point of maximum deflection. The error bars shown in the plot are derived from the standard deviation of the movement of the reference histogram for all applied voltages. The reference should theoretically stay constant but moves slightly, e.g. due to movement of the sample holder in the AFM.

4.4 Observation of Deflection by Non-Radiative Energy Transfer

To observe the change of excited state lifetime induced by graphene near quantum dots, lifetime measurements were performed while applying a backgate voltage to the sample, as previously described in Fig. 3.6. For measurements of single points, the lifetime histograms obtained can be directly compared to observe differences in the decay behaviour. For example, a series of lifetime measurements was performed at a point on the central ring of the BullsEye structure with a trench width of 750 nm. The measurement position is shown in a PL scan in Fig. 39a, it was verified before that there the graphene is suspended there using the AFM scan in Fig. 33a. After performing a series of scans at this point at various applied backgate voltages, the overall emission intensity, particularly at the scanned point decreases due to bleaching (see Fig. 39b).

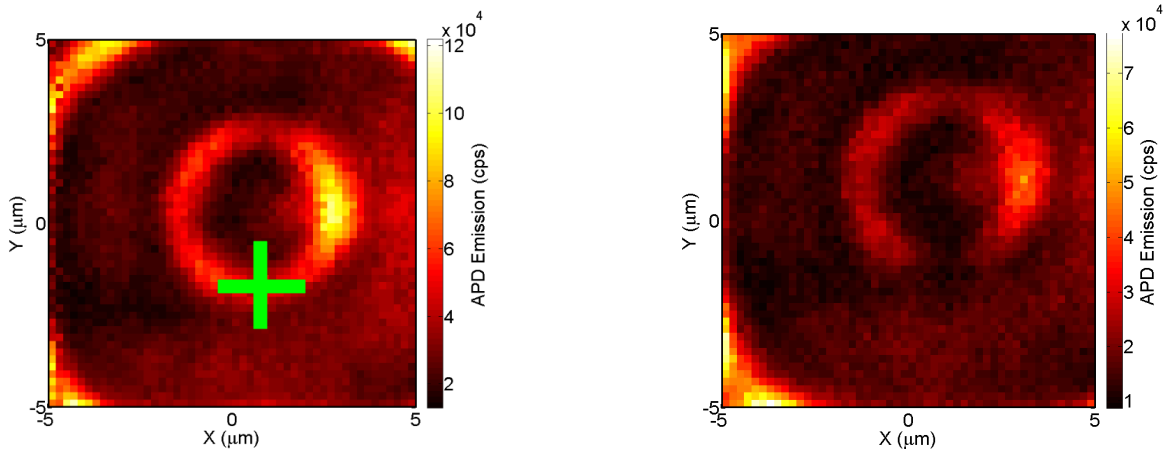

(a) (b)

Figure 39: PL scan of central ring of BullsEye structure before (a) and after (b) performing lifetime measurements. The lifetime was measured for various voltages at the point marked by the green cross, a decrease in emission intensity is visible there after the scans due to bleaching.

The lifetime histograms acquired are shown in Fig. 40. They were measured using a laser power of 10μW at a pulse repetition time of 200 ns and an integration time of 5 s per histogram. The deflection voltages here were chosen in the range of 0-10 V as the membrane is quite close to the trench bottom. A change in the short lifetimes is visible up to approximately 10 ns after the histogram peak. After applying 10 V, the voltage was slowly swept back to 0 V to see if the lifetime histogram returned back to its original shape. However, the decay after sweeping back to 0 V has the same shape

as that for an applied voltage of 10 V, this suggests that the membrane is stuck to the trench bottom.

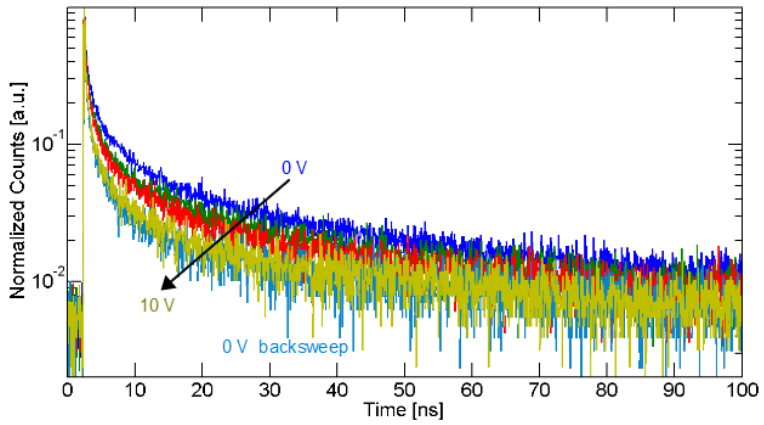

Figure 40: Lifetime histograms for a membrane on a trench structure with applied backgate voltages. The initial decay rate after the histogram maximum increases with the voltage applied, but fails to return to its initial rate when sweeping back to 0 V.

To confirm that the change in histogram shape is actually due to the applied voltage and not caused by the repeated measurements at the same point, a different membrane on the the lifetime was measured multiple times without applying a backgate voltage. The result of this is shown in Fig. 41 with the same scale as Fig. 40. Here, a small change of lifetime is observed with a progressive number of scans, the shape slightly changes due to a change in the fast decay after the histogram peak, this may be related to the bleaching also observable in the PL scans (see Fig. 39b). However, the degree of modification with a progressive scan number is less than the change with applied backgate voltage, for this reason it is presumed that the change in lifetime in Fig. 40 is caused by a movement of the graphene membrane towards the quantum dot layer.

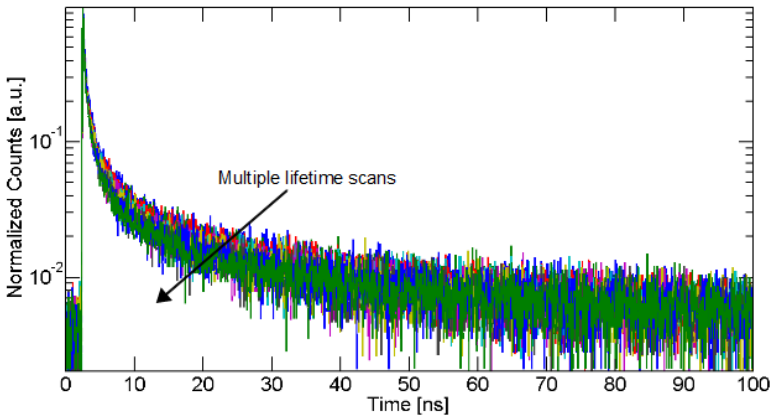

Figure 41: Transient behaviour of lifetime with multiple (10) scans of the same point on a suspended membrane. The number of scans progresses along the direction of the arrow. A slight increase of the initial decay rate is observed with a progressing number of scans.

While this development suggests that the graphene membrane moves and changes the lifetime of the quantum dots, it cannot be used to study or extract an actual distance dependence such as those proposed in the literature described previously. This due to the fact that neither the membrane shape nor the trench bottom are well defined. As has been shown, the membrane surroundings are not flat, causing it to deflect in an inhomogeneous way. Furthermore, peaks in the trench bottom can touch the membrane while it is deflected closer to the quantum dot layer, thus modifying its shape and therefore its deflection properties. These effects combined cause an unpredictable membrane deflection behaviour.

To measure the lifetime histograms across a larger area of the sample, a 2D scan can be performed where a histogram is acquired at each point. However, for 2D scans a point-by-point approach of comparing histograms is not a convenient method of analysis. Instead, we use a fit model of the quantum dot decay to visualize its transient emission upon excitation. A multi-exponential approach is chosen as it is well-established in the literature [57, 58, 59] that multi-excitons can be excited in quantum dots. This means that more than one exciton is created per incident photon and leads to a decay function that consists of the cumulative effect of each exciton decaying with an associated lifetime. For the case of the measurements performed for this thesis, a tri-exponential model was found to fit the experimental data well. The model is given by:

$$f(t) = a\,exp(\frac{-t}{\tau_1}) + b\,exp(\frac{-t}{\tau_2}) + c\,exp(\frac{-t}{\tau_3}) + f_0 \tag{5}$$

Fitting experimentally obtained histograms with this function allows the extraction of the three lifetimes τ_i, $i = 1, 2, 3$ and their associated exponential weighting a, b, c if the offset value f_0 is known - this is given by the dark counts of the APD that were measured for each set of histograms acquired. These lifetimes cover three regimes of decay: $\tau_1 \leqslant 1\,ns$, $1\,ns < \tau_2 \leqslant 10\,ns$ and $\tau_3 > 10\,ns$. The histograms acquired in the scan are fitted, and thus the value of each lifetime can be plotted to produce three lifetime and three amplitude maps. The fit results are visualized in Fig. 42a, where a histogram is shown on a semi-logarithmic scale with its tri-exponential fit. Three exemplary lifetimes are shown that can be used in the above model Eq. equation (5) to approximate the histogram. An example of the fit result is shown in 42b, where a measured histogram and its computed fit function show good agreement.

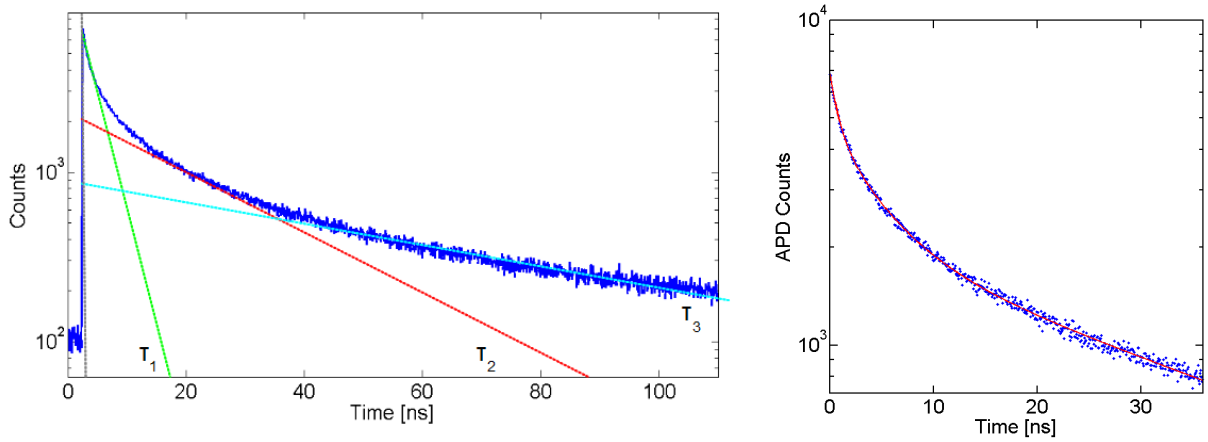

(a) (b)

Figure 42: Tri-exponential decay model: (a) Semi-logarithmic plot of a decay histogram with three lifetimes τ_i, $i = 1$, 2, 3, assumed to start at a time marked by the dashed, grey line. (b) Measured histogram (blue dots) of capped quantum dots with a fit (red line) computed by tri-exponential model. In this diagram, the dark count and time offset have been subtracted. The three lifetimes computed are $\tau_1 = 1.29\,ns$, $\tau_2 = 6.8\,ns$ and $\tau_3 = 48.2\,ns$.

Using the model described, 2D lifetime scans of a sample with suspended membranes on holes were performed. To locate the holes, an optical image of the hole array and a PL scan of the area of interest was used, both shown in Fig. 43. The two circular areas of high emission show the location of the membranes clearly in the PL scan.

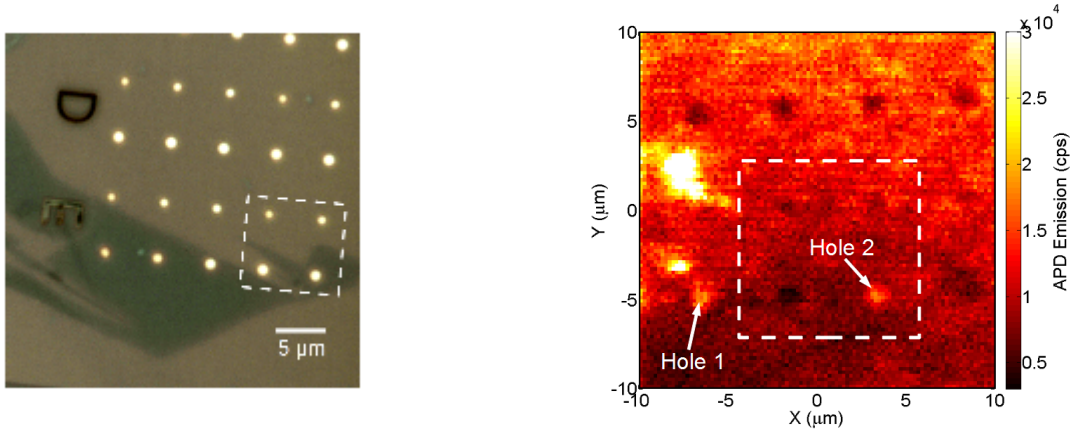

(a) (b)

Figure 43: Hole array partially covered by a graphene flake, consisting of rows of holes with diameters of 750 nm and 1μm. (a) Optical image showing the graphene flake (dark area) before contacting. The dashed square marks the area in which PL and lifetime scans were performed. (b) PL image of the contacted flake: horizontal rows of holes with lower emission intensity than their surroundings are visible. Two holes with suspended membranes of 1 μm diameter are clearly distinguishable due to their higher emission. The area scanned during the 2D lifetime scan is shown by the white dashed square.

During a square scan of 10 μm sidelength with 50 x 50 measurement points, lifetime histograms were obtained with 20 s integration time per point and a background level of 7 dark counts was recorded. The area chosen included a membrane, measured to be suspended 10 nm above the hole bottom by AFM scans. These histograms were fitted with the described model, resulting in 2D maps of lifetime and amplitude of their exponential function that are shown below in Fig. 44:

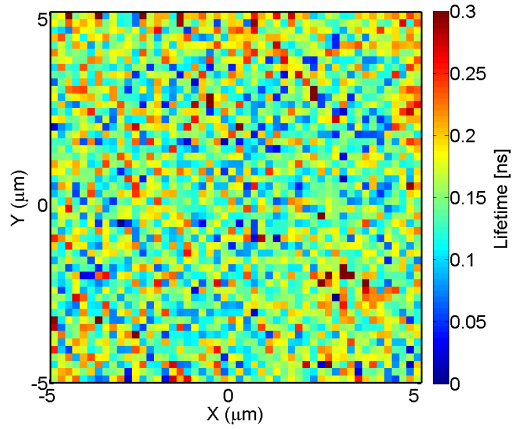

(a) τ_1

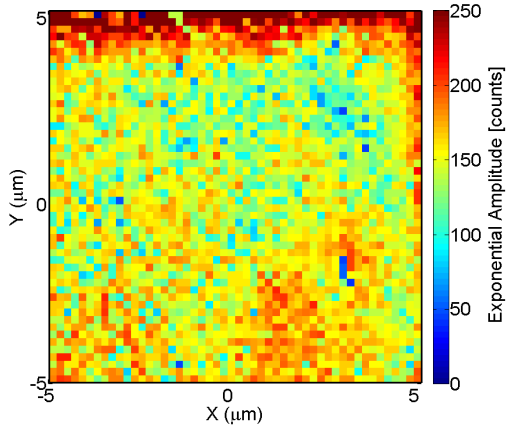

(b) Amplitude a

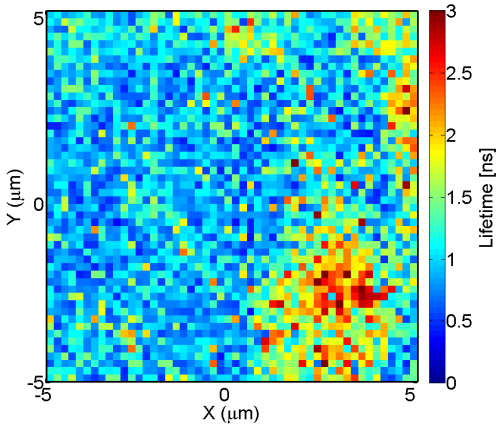

(c) τ_2

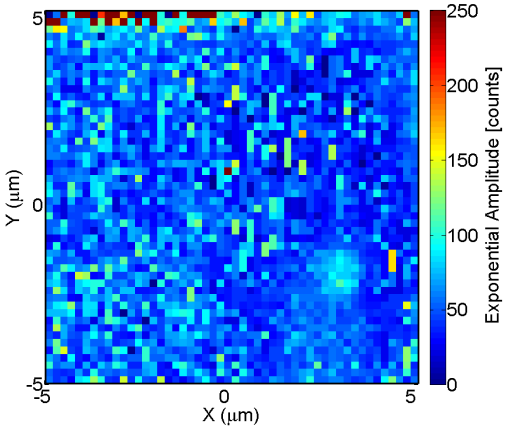

(d) Amplitude c

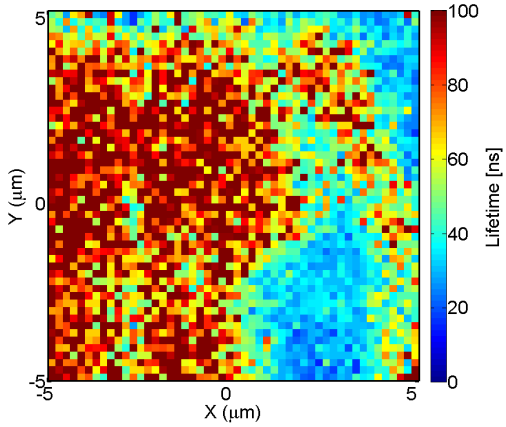

(e) τ_3

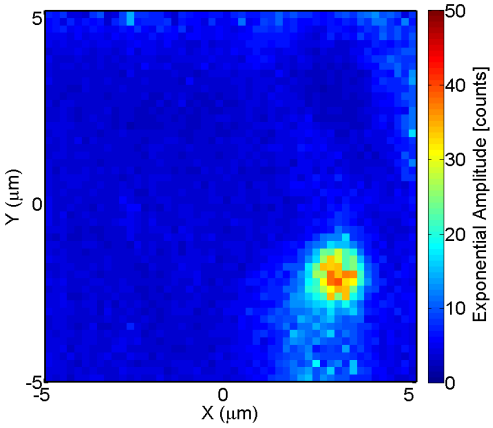

(f) Amplitude e

Figure 44: 2D maps of lifetimes τ_i, $i = 1, 2, 3$ (Figs. (a), (c) and (e)) with their corresponding amplitudes (Figs. (b), (d) and (f)) as given in Eq. 5. The amplitudes are plotted to the same scale to allow for a comparison of the respective weighting of each exponential component at a given point.

Of the three lifetimes shown in these images, τ_1 and especially τ_2 show an increase in the vicinity of the hole located at position (3,-2). This agrees with the concept of quenching by graphene: in the hole, the membrane is suspended some distance away from the quantum dot layer, resulting in less quenching and a longer lifetime, whereas outside it, the graphene lies very close to the emitters, thus reducing their lifetime. The holes in the scanned area that are not covered by a membrane are indistinguishable from the surface in the images, this suggests that the membrane has either collapsed there, or there is no graphene in that area.

However, comparing the respective amplitudes of the first two lifetimes, it is clear that the amplitude of τ_1 is in general higher over the whole area of the scan, but does not seem to be strongly dependent on the emitter-graphene separation as it takes on similar values in the hole area and away from it. Compared to this, the amplitude of τ_2 is in general lower, but shows a higher contrast to the surroundings in the hole area, thus it is more strongly affected by the graphene-emitter separation.

Finally, the longest lifetime τ_3 shows the opposite behaviour to the former two: it strongly decreases in the hole vicinity, while the generally low amplitude increases strongly only at the hole location but is still lower than both other amplitudes there. The lifetime reaches values of approximately 40 ns near the hole, compared to the surroundings where it takes on values of over 100 ns. Overall, τ_2 seems to best describe the behaviour of fluorescence quenching both on the substrate surface and in the hole area.

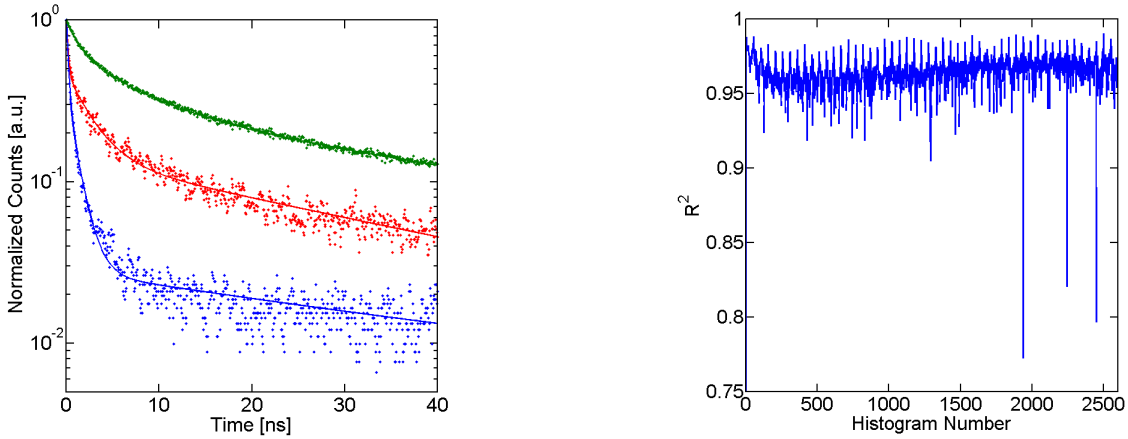

(a) (b)

Figure 45: (a) Comparison of measured (dots) and fitted (solid lines) normalised lifetime histograms of capped quantum dots on a substrate after a simulated transfer (green, see Fig. figure 27), quantum dots in Hole 2 shown in figure 43b (red) and quantum dots in an area outside the hole where they are directly covered by graphene (blue). The decay of capped quantum dots under suspended graphene and that of quantum dots not covered by graphene is similar except for the initial decay given by τ_1. In contrast, the decay of quantum dots directly covered by graphene is faster due to stronger quenching for small separations. (b) Coefficient of determination to measure the goodness of fit for the histogram data shown as a 2D map in figure 44, consisting of 2601 individual histograms.

To study whether τ_2 is indeed an indicator of the separation of the quantum dots to the graphene, fitted and normalised lifetime histograms of uncovered quantum dots after a simulated transfer (see Section **??**), directly covered quantum dots and quantum dots under suspended graphene are compared in Fig. figure 45a. Here, we see that the uncovered emitters and their counterparts under suspended graphene differ in their fastest decay, but the subsequent slower decay is similar in gradient, indicating that the lifetimes $\tau_2$and τ_3 are similar for both. The fastest decay and thus also the shortest lifetime τ_1 is affected by the transfer process as shown in figure 27, therefore the difference between the two curves is ascribed to a longer processing time in a real transfer than in the simulated one. Compared to the quantum dots under the suspended graphene and the uncovered layer, the decay of the directly covered layer is much faster for both the fastest and also subsequent slower decay, indicated by the high negative gradient of the blue histogram in Fig. figure 45a.

To quantify the lifetime differences, we use the tri-exponential fit also shown in Fig. figure 45a. This yields the following lifetimes in the order τ_1, τ_2, τ_3: 1.1 ns, 6.8 ns, 48 ns

for the uncovered quantum dots; 0.17 ns, 2.6 ns, 33 ns for the quantum dots under the membrane and 0.2 ns, 1.1 ns, 44 ns for the quantum dots outside the hole, directly covered by graphene. Therefore, τ_1 is similar for the emission inside and outside the hole, but lower than for the uncovered quantum dots due to the difference between a real and a simulated graphene transfer. The lifetime τ_3 is similar for directly covered and completely uncovered dots, indicating that it is not strongly affected by the presence of graphene as discussed previously. Finally, τ_2 is highest for uncovered quantum dots, and reduces with increasing proximity of graphene from a separation of approximately 10 nm of the membrane and quantum dot layer to its lowest value for the case of closest possible contact where graphene is directly on the capping layer. This suggests that τ_2 is an indicator of the emitter-graphene separation.

To be able to use a map of lifetime as a reliable indicator of the graphene-emitter separation requires the tri-exponential model to fit the data well across the scanned area, implying a high goodness of fit for all histograms acquired. A measure of this is given by the coefficient of determination R^2 of the fit, with $R^2 = 1$ for a perfect fit. It is given by the square of the correlation coefficient which describes the correlation of the given and the fitted data (see [60]). The value of R^2 for each of the 2601 histograms fitted to obtain the lifetime and amplitude maps in Fig. figure 44 is shown in Fig. figure 45b, where the average value of 0.96 shows that the data is fitted well over the area of the scan.

To detect changes in the lifetime of the quantum dots under the suspended membrane with an applied backgate voltage, line traces of lifetime were made across the covered hole and its surroundings while applying backgate voltages up to 5 V. This small range of voltages compared to the previously described range of 0-50 V was chosen to avoid the membrane sticking to the hole bottom. For each applied voltage, 50 histograms were acquired along a 10 μm scan length with an integration time of 15 s. The line scan location is shown on a PL image in Fig. 46a, taken after multiple scan cycles. The line is clearly visible due to emission bleaching as this sample was measured before the capping layers were used to protect the quantum dot layers. In the image, the line appears broader than the actual laser spot size due to small movements of the sample during measurements.

Each acquired histogram was fitted to a tri-exponential decay to obtain three lifetimes at each scan point. As for the 2D lifetime scan described previously, the lifetime in the range of 1-10 ns (τ_2) was found to fit the physical situation of higher lifetime of the emitters at a distance away from the membrane in the hole compared to the lifetime of emitters directly under the graphene. To detect a change in lifetime with applied backgate voltage, an average of τ_2 was taken over the hole region and compared to an

average taken over an area on the substrate. This is shown in Fig. 46:

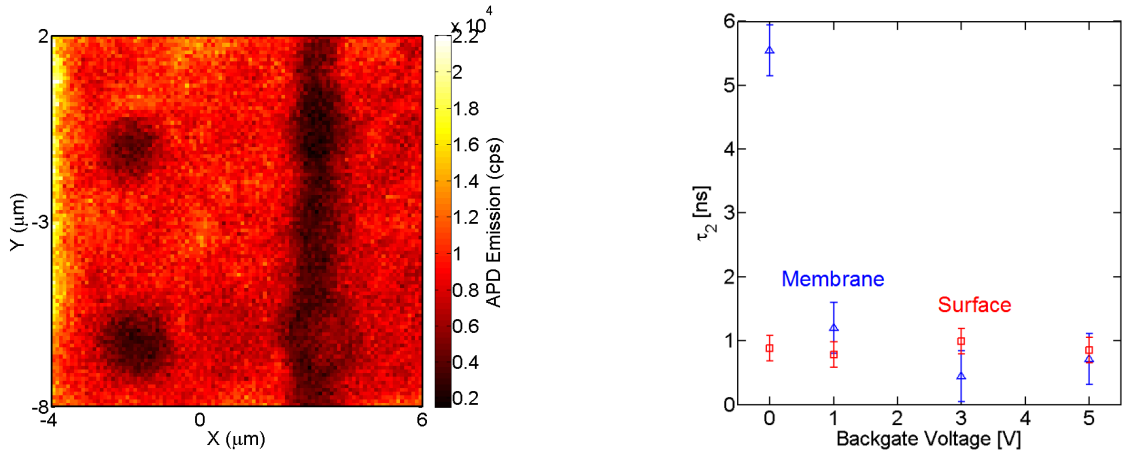

(a) (b)

Figure 46: Lifetime linescan over a suspended circular membrane with applied backgate voltage: (a) PL image of part of the hole array including the membrane, taken after multiple linescans. The linescan location is clearly visible as a dark vertical line due to bleaching of the quantum dots, with the dark line being slightly broader than the laser spot size due to small movements of the sample during measurement. (b) Fitted mean lifetime τ_2 of quantum dots below a suspended graphene membrane (blue triangles) and on the substrate surface (red squares) plotted against applied backgate deflection voltage. An average of lifetime is taken over the membrane area and compared to the change of lifetime on the substrate to see the effect of lifetime change with voltage. The error bars are derived from the 95 % confidence interval of the tri-exponential fit.

Comparing the average lifetimes at 0 V, it is clear that there is a large difference in emitter lifetime below the suspended membrane and on the surface, where the graphene is almost in contact with the emitters. However, this difference is strongly reduced upon application of a backgate voltage of 1 V and above, where the lifetimes are almost identical. It appears that the membrane was already very close to the hole bottom before deflection, and therefore required only a small voltage to deflect it to an extent where it touches the hole bottom, which is irreversible due to van der Waals forces that cause the graphene and substrate to become strongly attached to each other. While this result suggests that the membrane moved, it again does not yield a reproduceable voltage control, and many more data points would be required to confirm this. More measurements were performed on other samples with suspended graphene, however their emission intensity was too low to detect a lifetime change.

5 Conclusion and Outlook

5.1 Conclusion

In this work, it was shown that the movement of a suspended graphene membrane over fluorescent quantum dots can be detected by measurement of their excited state lifetime. This is based on resonant energy transfer from excited dipoles in the quantum dots to dipoles in graphene. To demonstrate this, graphene flakes were suspended over hole and trench structures in silicon dioxide coated with thin films of PbS quantum dots. The graphene membrane formed in this way was actuated electrostatically by application of a backgate voltage between the flake and a doped silicon substrate on which the hole and trench structures were fabricated.

Initially, the topology of the membranes and coated substrate surface was studied using atomic force microscopy, this data being used to optimize the structure of the samples so that the graphene membrane is suspended above the quantum dot layer at a distance sufficiently large to be able to see changes of excited state lifetime of the emitter while avoiding direct contact between the membrane and emitter. The emission of the coated substrates partially covered by a graphene flake was studied, and it was found that the location of the flake can be determined by scanning photoluminescence measurements due to its quenching of the emitter fluorescence and comparing this to AFM measurements.

Furthermore, the emission properties of quantum dot films exposed to atmospheric oxygen, humidity as well as to the chemicals involved in the graphene transfer were studied. It was found that all of these factors are detrimental to both the emission intensity as well as the excited state lifetime of the quantum dots. The change of excited state lifetime caused by these factors was found to affect different transient regimes of the emitter decay. The degree of modification of the decay properties of the emitters was found to be on the order of that to be expected by graphene fluorescence quenching. For this reason, thin capping layers of silicon dioxide were deposited on samples coated with quantum dots by evaporation, thus protecting them and providing more reliable samples with less bleaching.

In subsequent topology measurements, it was found that the capped quantum dot layer on the samples as well as the graphene membranes themselves were very rough, thus preventing an precise determination of the membrane-emitter separation. For this reason, a statistical approach was used to find the degree deflection of suspended membranes under application of an electrostatic force. Histograms of height distribution for different voltages in the membrane area were compared to a reference point on the

sample surface, thus allowing the mean deflection of the membrane to be determined. It was also verified that the membrane returns to its original position with no applied voltage. The deflection was found to match theoretically values predicted by a thin plate capacitor model quite well for 750 nm diameter membranes. Other membranes were also studied without detection of deflection. This is attributed to their strong wrinkling, causing most of the deflecting force to change the membrane shape without any resulting net deflection of the entire membrane.

To detect changes of emitter lifetime caused by resonant energy transfer to graphene, membranes on a trench structure were actuated electrostatically. Using a time correlated photon counting method, the excited state lifetimes of the emitters were determined and found to decrease with increasing backgate voltage. To verify this, the change of lifetime due to subsequent scans was studied and found to be weaker than that observed with applied backgate voltages, suggesting that the origin of the lifetime change is distant-dependent fluorescence quenching by graphene. However, the actual distance dependence could not be determined as the trench structure and membrane are too rough and inhomogeneous to allow for accurate control of the membrane-emitter separation.

Maps of the excited state lifetime across areas of the samples were obtained from 2D lifetime scans. The resulting histograms were fitted using a tri-exponential decay model to extract amplitudes of each exponent and the associated lifetimes at each measurement point, based on the multi-exitonic decay of quantum dots well known from the literature. It was observed that the location of suspended membranes was most visible in maps of lifetime in the range of 1-10 ns, where both the amplitude and lifetime were higher compared to the surroundings in direct contact with the graphene, thus being in agreement with the notion of distant dependent quenching. Lifetimes shorter than 1 ns appeared to be only weakly affected by the difference between graphene suspended over the quantum dot layer or in direct contact with it. On the other hand, long lifetimes in the regime longer than 10 ns were seen to decrease together with their intensity in the membrane area. This behaviour is not yet fully understood, as it is the opposite behaviour to the theoretically predicted one. Overall, the dominant lifetime in terms of amplitude behaves as predicted theoretically

One-dimensional lifetime linescans across the suspended membrane with applied backgate voltages were also performed after verification of longer lifetime in the membrane area by 2D lifetime scans. A change of lifetime with applied backgate voltage was observed, however only few data could be gathered as the membrane seems to have stuck to the hole bottom as soon as a small voltage was applied, inhibiting further study of the deflection dependence. Other samples were studied, but low emission levels due

to strong bleaching prevented multiple lifetime measurements to be performed.

In conclusion, the results of this thesis show that it is in principle possible to optically detect the motion of a graphene membrane suspended over quantum dots. The samples made so far did not allow for an accurate determination of the distance dependence due to their inhomogeneous surface structure both inside and outside the hole and trench structures fabricated. Nonetheless, the work done provides a basis for further studies of graphene nano-resonators combined with fluorescent emitters as many fundamental issues in their fabrication and the measurement of distant-dependent quenching have been identified and solutions have been proposed.

5.2 Outlook

The first step to be considered for further investigation of distant-dependent quenching is the fabrication of reliable and homogeneous membranes on support structures to provide a clean system to ensure accurate and reproducible measurements. One approach towards this is to separate the membrane support and emitter structures. The fabrication of this kind of two-component nano-resonator has been demonstrated experimentally [61]: a membrane structure on a hole in an etched substrate is fabricated separately from the emitter layer. This membrane structure is then placed on to a separate substrate that is coated with a thin layer of fluorescent emitters such as dye molecules. This has the advantage that the support structure for the graphene is very smooth as it is directly transferred to the etched substrate, with the possibility of using CVD graphene to cover the entire surface of the membrane support area, yielding a large number of membranes per sample. Furthermore, the graphene can be heat-treated to make it smoother on the surface [62], without damaging the emitter layer. The emitter layer can be made very thin so that the emission of only a single layer is considered without any depth effects that can decrease the resolution of the distance dependence (see [22]). A further advantage is that the graphene membranes made in this way can be re-used: if the emitter layer bleaches, it can be replaced by a fresh one without having to make a completely new sample.

With a sample fabricated in this way, it should be possible to study the behaviour of the drum structure when driven by an oscillating backgate voltage. At its resonance frequency, the membrane should give a strong response due to the typically large quality (Q) -factor of graphene nano-resonators well above 1000 [63, 61, 15]. This should also be detectable optically, as the high Q-factor causes the membrane to be oscillate strongly over a very narrow frequency range around the resonance frequency. Due to the non-linearity of the distance-dependence of fluorescence quenching, one can expect

a measurable shift in the average emission from the emitters when the amplitude of oscillation reaches a maximum at resonance.

With a functioning nano-resonator on emitters, the emerging field of optomechanics would have a new structure to investigate fundamental physics. For example, it is theoretically feasible that a single emitter placed inside a graphene nano-resonator could cool down the graphene lattice to its ground state by Doppler cooling - this has been theoretically proposed but not shown experimentally so far [13]. Finally, more practical applications such as ultra-sensitive mass and pressure sensors that could be read out optically are also possible. Overall, the combination of the optoelectronic and mechanical properties of graphene in these devices have many fundamental studies and practical applications still to be discovered.

6 Acknowledgements

I am very grateful to Frank Koppens as supervisor and Uli Lemmer as co-supervisor to have made this thesis possible, giving me a great opportunity and the support to work on an emerging field at an institute where the frontiers of photonics are being pushed that little bit further every day. My thanks goes to everyone at ICFO who makes it happen, especially those who helped me with my project by providing me with advice and materials.

Muchas gracias à Maria Bernechea for manufacturing and providing the PbS quantum dots, Silke Diedenhofen for measuring their emission spectrum and Alex Stavrinadis for providing extensive answers to the many questions I had about the properties of quantum dots, as well as many others who would drop a long sought-after hint over a coffee, or while out for a break in the shade of the institute. I am indebted to the teams from the mechanical and electrical workshops that provided fast and reliable constructions often based on back-of-the-envelope sketches. Merci à Johann Osmond for showing me all the tweaks of making a nice AFM image and helping me when things went awry, for example by asking "have you tried turning it off and on again?" - surprisingly, this even works for such a complicated device. Carme Gómez introduced me to the perils of working with the wire bonder, and many a time she brought me out of the dire straits of coping with it in her cheerful, good-natured way. In general, my thanks goes to all support staff at ICFO, including IT and Human Resources, who are always there in the background oiling and tweaking the screws of the big and bustling engine which ICFO is every day.

My special thanks goes to Louis Gaudreau, my mentor who went to great lengths in getting me acquainted with all the setups and fabrication processes, and supported me with advice and patience during my thesis. His supervision style was like that of a good guide star: there to set me in the right direction when I needed it, while still letting me do things in the way I thought to be right. As is in the nature of being a guide star, he is also a bit through the roof at times, which made working with him all the more fun. With time, I am happy to say that we have become good companions both in the lab and outside, which is something I would not take for granted and therefore I am all the more grateful for it.

Special mention must also go to Gabriele who worked with me in making the samples by making the structures on the substrate with the FIB and by taking charge of the graphene transfer. In both of these processes, she spent countless hours and acquired much expertise in fabrication, without which the experiments in this thesis would not have been possible, making her an essential ingredient of my work that I am much

indebted to. She was also a good companion to have during long evenings and weekends of thesis-writing. I would also like to thank Klaas, who gave me plenty of advice and taught me a few tricks of the trade in data analysis. It was he who pointed me towards the ideas of how best to extract the essential information in some of the data I gathered, and one more than one occasion he saved me from having (multi-exponential) fits in the process.

Finally, I want to thank my group of weird and wonderful co-workers: Marko for his dry wit that made being in office 223 a good laugh, Achim and Fabio for (refreshingly unscientific) chats over a cigarette in the good times and the bad, Simon for taking care I didn't run low on caffeine, absurd jokes and considerations of momentum storage in English roundabouts, Ivan and Michela for the odd bike rental that saved me from tedious hikes up the Castelldefelsian mountains and all of my fellow Master students at ICFO whom I shared many a good time with, and whose mutual support made getting through thesis writing that bit more enjoyable. Overall, it is really the people here that make this place a special one, and it is great that the sense of belonging together extends beyond the lab doors. I am very happy I decided to do my thesis here, even if it may have left me:

"Insane in the membrane, insane in the brain!" - Cypress Hill

Luckily, my friends and family kept me from this by their encouragement and support when the going got tough, which I am very grateful for - it is that which has kept me going so far, and will continue to do so.

References

[1] K. S. Novoselov, A. K. Geim, S. V. Morozov, D. Jiang, Y. Zhang, S. V. Dubonos, I. V. Grigorieva, and A. A. Firsov. Electric field effect in atomically thin carbon films. *Science*, 306(5696):666–669, 2004.

[2] Gerasimos Konstantatos, Michela Badioli, Louis Gaudreau, Johann Osmond, Maria Bernechea, F. Pelayo Garcia de Arquer, Fabio Gatti, and Frank H. L. Koppens. Hybrid graphene-quantum dot phototransistors with ultrahigh gain. *Nat Nano*, 7(6):363–368, June 2012.

[3] Y.-M. Lin, C. Dimitrakopoulos, K. A. Jenkins, D. B. Farmer, H.-Y. Chiu, A. Grill, and Ph. Avouris. 100-ghz transistors from wafer-scale epitaxial graphene. *Science*, 327(5966):662, 2010.

[4] F. Bonaccorso, Z. Sun, T. Hasan, and A. C. Ferrari. Graphene photonics and optoelectronics. *Nat Photon*, 4(9):611–622, September 2010.

[5] Xuesong Li, Weiwei Cai, Jinho An, Seyoung Kim, Junghyo Nah, Dongxing Yang, Richard Piner, Aruna Velamakanni, Inhwa Jung, Emanuel Tutuc, Sanjay K. Banerjee, Luigi Colombo, and Rodney S. Ruoff. Large-area synthesis of high-quality and uniform graphene films on copper foils. *Science*, 324(5932):1312–1314, 2009.

[6] Xu Du, Ivan Skachko, Anthony Barker, and Eva Y. Andrei. Approaching ballistic transport in suspended graphene. *Nat Nano*, 3(8):491–495, August 2008.

[7] K. S. Novoselov, Z. Jiang, Y. Zhang, S. V. Morozov, H. L. Stormer, U. Zeitler, J. C. Maan, G. S. Boebinger, P. Kim, and A. K. Geim. Room-temperature quantum hall effect in graphene. *Science*, 315(5817):1379, 2007.

[8] A. K. Geim and K. S. Novoselov. The rise of graphene. *Nat Mater*, 6(3):183–191, March 2007.

[9] K. S. Novoselov, A. K. Geim, S. V. Morozov, D. Jiang, M. I. Katsnelson, I. V. Grigorieva, S. V. Dubonos, and A. A. Firsov. Two-dimensional gas of massless dirac fermions in graphene. *Nature*, 438(7065):197–200, November 2005.

[10] R. R. Nair, P. Blake, A. N. Grigorenko, K. S. Novoselov, T. J. Booth, T. Stauber, N. M. R. Peres, and A. K. Geim. Fine structure constant defines visual transparency of graphene. *Science*, 320(5881):1308, 2008.

[11] Changgu Lee, Xiaoding Wei, Jeffrey W. Kysar, and James Hone. Measurement of the elastic properties and intrinsic strength of monolayer graphene. *Science*, 321(5887):385–388, 2008.

[12] C-L Wong, M Annamalai, Z-Q Wang, and M Palaniapan. Characterization of nanomechanical graphene drum structures. *Journal of Micromechanics and Microengineering*, 20(11):115029, 2010.

[13] Menno Poot and Herre S.J. van der Zant. Mechanical systems in the quantum regime. *Physics Reports*, 511(5):273 – 335, 2012. <ce:title>Mechanical systems in the quantum regime</ce:title>.

[14] I. W. Frank, D. M. Tanenbaum, A. M. van der Zande, and P. L. McEuen. Mechanical properties of suspended graphene sheets. volume 25, pages 2558–2561. AVS, 2007.

[15] Changyao Chen, Sami Rosenblatt, Kirill I. Bolotin, William Kalb, Philip Kim, Ioannis Kymissis, Horst L. Stormer, Tony F. Heinz, and James Hone. Performance of monolayer graphene nanomechanical resonators with electrical readout. *Nat Nano*, 4(12):861–867, December 2009.

[16] G. Gomez-Santos and T. Stauber. Fluorescence quenching in graphene: A fundamental ruler and evidence for transverse plasmons. *Phys. Rev. B*, 84:165438, Oct 2011.

[17] Haixin Chang, Longhua Tang, Ying Wang, Jianhui Jiang, and Jinghong Li. Graphene fluorescence resonance energy transfer aptasensor for the thrombin detection. *Anal. Chem.*, 82(6):2341–2346, February 2010.

[18] Haifeng Dong, Wenchao Gao, Feng Yan, Hanxu Ji, and Huangxian Ju. Fluorescence resonance energy transfer between quantum dots and graphene oxide for sensing biomolecules. *Anal. Chem.*, 82(13):5511–5517, June 2010.

[19] Zheyuan Chen, Stephane Berciaud, Colin Nuckolls, Tony F. Heinz, and Louis E. Brus. Energy transfer from individual semiconductor nanocrystals to graphene. *ACS Nano*, 4(5):2964–2968, 2010. PMID: 20402475.

[20] R. S. Swathi and K. L. Sebastian. Resonance energy transfer from a dye molecule to graphene. *The Journal of Chemical Physics*, 129(5):054703, 2008.

[21] R.S. Swathi and K.L. Sebastian. Long range resonance energy transfer from a dye molecule to graphene has (distance)$^{-}$4 dependence. *jcp*, 130(8):086101, February 2009.

[22] L. et al. Gaudreau. Graphene reveals universal scaling of light-matter interaction. 2012.

[23] Arend M. van der Zande, Robert A. Barton, Jonathan S. Alden, Carlos S. Ruiz-Vargas, William S. Whitney, Phi H. Q. Pham, Jiwoong Park, Jeevak M. Parpia, Harold G. Craighead, and Paul L. McEuen. Large-scale arrays of single-layer graphene resonators. *Nano Letters*, 10(12):4869–4873, 2010.

[24] A. M. v. d. Zande. *The Structure and Mechanics of Atomically-Thin Graphene Membranes*. PhD thesis, Cornell University, 2011.

[25] A. H. Castro Neto, F. Guinea, N. M. R. Peres, K. S. Novoselov, and A. K. Geim. The electronic properties of graphene. *Rev. Mod. Phys.*, 81:109–162, Jan 2009.

[26] Nageswara Ghattamaneni Benjamin Harack Michael Hilke Alexandre Horth Norberto Majlis Mathieu Massicotte Leron Vandsburger Eric Whiteway Victor Yu Daniel R. Cooper, Benjamin D'Anjou. Experimental review of graphene. Unpublished, available on arXiv, October 2011.

[27] P. R. Wallace. The band theory of graphite. *Phys. Rev.*, 71:622–634, May 1947.

[28] R. E. Peierls. Quelques proprietes typiques des corpses solides. *Ann. Inst. Henri Poincare*, 5:177,222, 1935.

[29] K.I. Bolotin, K.J. Sikes, Z. Jiang, M. Klima, G. Fudenberg, J. Hone, P. Kim, and H.L. Stormer. Ultrahigh electron mobility in suspended graphene. *Solid State Communications*, 146(9-10):351 – 355, 2008.

[30] Enrico Fermi. Quantum theory of radiation. *Rev. Mod. Phys.*, 4:87–132, Jan 1932.

[31] W.L. Barnes. Fluorescence near interfaces: the role of photonic mode density. *Journal of Modern Optics*, 45(4):661–699, 1998.

[32] Mark Fox. *Quantum Optics - An Introduction*. Oxford University Press, 2006.

[33] Karl H. Drexhage. Iv interaction of light with monomolecular dye layers. volume 12 of *Progress in Optics*, pages 163 – 232. Elsevier, 1974.

[34] Sergey V. Gaponenko. *Introduction to Nanophotonics*. Cambridge University Press, 2010.

[35] Th. Förster. Zwischenmolekulare energiewanderung und fluoreszenz. *Annalen der Physik*, 437(1-2):55–75, 1948.

[36] Paul R. Selvin. The renaissance of fluorescence resonance energy transfer. *Nature Structural & Molecular Biology*, 7(9):730–734, September 2000.

[37] B. N. J. Persson and N. D. Lang. Electron-hole-pair quenching of excited states near a metal. *Phys. Rev. B*, 26:5409–5415, Nov 1982.

[38] Qiaoliang Bao and Kian Ping Loh. Graphene photonics, plasmonics, and broadband optoelectronic devices. *ACS Nano*, 6(5):3677–3694, April 2012.

[39] Jianing Chen, Michela Badioli, Pablo Alonso-Gonzalez, Sukosin Thongrattanasiri, Florian Huth, Johann Osmond, Marko Spasenovic, Alba Centeno, Amaia Pesquera, Philippe Godignon, Amaia Zurutuza Elorza, Nicolas Camara, F. Javier Garcia de Abajo, Rainer Hillenbrand, and Frank H. L. Koppens. Optical nano-imaging of gate-tunable graphene plasmons. *Nature*, 487(7405):77–81, July 2012.

[40] Y. Huang, J. Wu, and K. C. Hwang. Thickness of graphene and single-wall carbon nanotubes. *Phys. Rev. B*, 74:245413, Dec 2006.

[41] J. Scott Bunch, Scott S. Verbridge, Jonathan S. Alden, Arend M. van der Zande, Jeevak M. Parpia, Harold G. Craighead, and Paul L. McEuen. Impermeable atomic membranes from graphene sheets. *Nano Letters*, 8(8):2458–2462, 2008. PMID: 18630972.

[42] A J Gil, S Adhikari, F Scarpa, and J Bonet. The formation of wrinkles in single-layer graphene sheets under nanoindentation. *Journal of Physics: Condensed Matter*, 22(14):145302, 2010.

[43] Iwan Moreels, Karel Lambert, Dries Smeets, David De Muynck, Tom Nollet, Jose C. Martins, Frank Vanhaecke, Andrei Vantomme, Christophe Delerue, Guy Allan, and Zeger Hens. Size-dependent optical properties of colloidal pbs quantum dots. *ACS Nano*, 3(10):3023–3030, 2009. PMID: 19780530.

[44] Jeffrey J. Peterson and Todd D. Krauss. Fluorescence spectroscopy of single lead sulfide quantum dots. *Nano Letters*, 6(3):510–514, 2006.

[45] M.A. Hines and G.D. Scholes. Colloidal pbs nanocrystals with size-tunable near-infrared emission: Observation of post-synthesis self-narrowing of the particle size distribution. *Advanced Materials*, 15(21):1844–1849, 2003.

[46] Jeffrey J. Peterson and Todd D. Krauss. Photobrightening and photodarkening in pbs quantum dots. *Phys. Chem. Chem. Phys.*, 8(33):3851–3856, 2006.

[47] Milan Sykora, Alexey Y. Koposov, John A. McGuire, Roland K. Schulze, Olexandr Tretiak, Jeffrey M. Pietryga, and Victor I. Klimov. Effect of air exposure on surface properties, electronic structure, and carrier relaxation in pbse nanocrystals. *ACS Nano*, 4(4):2021–2034, 2010. PMID: 20369900.

[48] Rachelle Ihly, Jason Tolentino, Yao Liu, Markelle Gibbs, and Matt Law. The photothermal stability of pbs quantum dot solids. *ACS Nano*, 5(10):8175–8186, 2011.

[49] G. Binnig, C. F. Quate, and Ch. Gerber. Atomic force microscope. *Phys. Rev. Lett.*, 56:930–933, Mar 1986.

[50] Franz J. Giessibl. Advances in atomic force microscopy. *Rev. Mod. Phys.*, 75:949–983, Jul 2003.

[51] Bruker AFM Probes. Manufacturer's website:.

[52] K. S. Novoselov, D. Jiang, F. Schedin, T. J. Booth, V. V. Khotkevich, S. V. Morozov, and A. K. Geim. Two-dimensional atomic crystals. *Proceedings of the National Academy of Sciences of the United States of America*, 102(30):10451–10453, 2005.

[53] Gabriele Navickaite. Fabrication and characterization of graphene nanostructures. Master's thesis, Institute of Photonic Sciences, Barcelona, 2012.

[54] Cecilia Mattevi, Hokwon Kim, and Manish Chhowalla. A review of chemical vapour deposition of graphene on copper. *J. Mater. Chem.*, 21(10):3324–3334, 2011.

[55] K. S. Novoselov. Nobel lecture: Graphene: Materials in the flatland. *Rev. Mod. Phys.*, 83:837–849, Aug 2011.

[56] Chun Hung Lui, Kin Fai Mak, Jie Shan, and Tony F. Heinz. Ultrafast photoluminescence from graphene. *Phys. Rev. Lett.*, 105:127404, Sep 2010.

[57] Oleg V. Prezhdo. Multiple excitons and the electron-phonon bottleneck in semiconductor quantum dots: An ab initio perspective. *Chemical Physics Letters*, 460(13):1 – 9, 2008.

[58] Randy J. Ellingson, Matthew C. Beard, Justin C. Johnson, Pingrong Yu, Olga I. Micic, Arthur J. Nozik, Andrew Shabaev, and Alexander L. Efros. Highly efficient multiple exciton generation in colloidal pbse and pbs quantum dots. *Nano Letters*, 5(5):865–871, 2005.

[59] Arthur J. Nozik. Multiple exciton generation in semiconductor quantum dots. *Chemical Physics Letters*, 457(1-3):3 – 11, 2008.

[60] Joseph Lee Rodgers and W. Alan Nicewander. Thirteen ways to look at the correlation coefficient. *The American Statistician*, 42(1):59–66, February 1988.

[61] Robert A. Barton, B. Ilic, Arend M. van der Zande, William S. Whitney, Paul L. McEuen, Jeevak M. Parpia, and Harold G. Craighead. High, size-dependent quality factor in an array of graphene mechanical resonators. *Nano Letters*, 11(3):1232–1236, 2011.

[62] C. R. et al. Dean. Boron nitride substrates for high-quality graphene electronics. *Nat Nano*, 5(10):722–726, October 2010.

[63] V. Adiga, R. Ilic, R. Barton, J. Parpia, and H. Craighead. Ultrathin circular membranes with high quality factors. In *APS March Meeting Abstracts*, page 7006, February 2012.